

Siena Galaxy Atlas 2020

JOHN MOUSTAKAS,¹ DUSTIN LANG,² ARJUN DEY,³ STÉPHANIE JUNEAU,³
AARON MEISNER,³ ADAM D. MYERS,⁴ EDWARD F. SCHLAFLY,⁵
DAVID J. SCHLEGEL,⁶ FRANCISCO VALDES,³ BENJAMIN A. WEAVER,³ AND
RONGPU ZHOU⁶

¹*Department of Physics and Astronomy, Siena College, 515 Loudon Road, Loudonville, NY 12110, USA*

²*Perimeter Institute for Theoretical Physics, 31 Caroline Street North, Waterloo, ON N2L 2Y5, Canada*

³*NSF's NOIRLab, 950 N. Cherry Avenue, Tucson, AZ 85719, USA*

⁴*Department of Physics and Astronomy, University of Wyoming, Laramie, WY 82071, USA*

⁵*Space Telescope Science Institute, 3700 San Martin Drive, Baltimore, MD 21218, USA*

⁶*Lawrence Berkeley National Laboratory, 1 Cyclotron Road, Berkeley, CA 94720, USA*

Submitted to ApJS

ABSTRACT

We present the 2020 version of the Siena Galaxy Atlas (SGA-2020), a multi-wavelength optical and infrared imaging atlas of 383,620 nearby galaxies. The SGA-2020 uses optical *grz* imaging over $\approx 20,000$ deg² from the DESI Legacy Imaging Surveys Data Release 9 and infrared imaging in four bands (spanning 3.4–22 μm) from the six-year unWISE coadds; it is more than 95% complete for galaxies larger than $R(26) \approx 25''$ and $r < 18$ measured at the 26 mag arcsec⁻² isophote in the *r*-band. The atlas delivers precise coordinates, multi-wavelength mosaics, azimuthally averaged optical surface brightness profiles, model images and photometry, and additional ancillary metadata for the full sample. Coupled with existing and forthcoming optical spectroscopy from the Dark Energy Spectroscopic Instrument (DESI), the SGA-2020 will facilitate new detailed studies of the star formation and mass assembly histories of nearby galaxies; enable precise measurements of the local velocity field via the Tully-Fisher and Fundamental Plane relations; serve as a reference sample of lasting legacy value for time-domain and multi-messenger astronomical events; and more.

1. INTRODUCTION

1.1. *Scientific Context*

Although a broad theoretical framework exists for understanding the physics of galaxy formation, many key questions remain unanswered. In this framework, the star formation and stellar mass assembly histories of galaxies are intimately linked to the hierarchical buildup of dark matter halos, modulated by a time-varying interplay between internal (secular) and external (environmental) processes (e.g., Kennicutt 1998; Kormendy & Kennicutt 2004; Blanton & Moustakas 2009; Somerville & Davé 2015; Naab & Ostriker 2017; Wechsler & Tinker 2018). Identifying these physical processes and their relative importance—as a function of cosmic time—remains one of the foremost outstanding problems in observational cosmology.

Some of the most pressing outstanding questions include:

- How and why does star formation in galaxies cease? Why do low-mass galaxies exhibit more extended star formation histories than massive galaxies?
- What is the nature of inside-out galaxy formation—did galaxies start growing earlier in their inner parts, did they end star-formation earlier in those parts, or both?
- How does feedback from active galactic nuclei, supernovae, stellar winds, and other effects regulate star formation?
- What was the relative impact of mergers versus secular processes on the structure of present-day galaxies, including their bulges, bars, spirals, rings, warps, shells, and pseudobulges?
- How are all these detailed processes affected by the relationship between galaxies and their host dark matter halo—for example, whether they are central or satellite galaxies?

Investigating these and related questions requires an accurate and detailed view of the present-day galaxy population—the population we can potentially understand the best. In particular, galaxies which are near enough or intrinsically large enough in terms of their apparent angular diameter to be spatially well-resolved can be studied in significantly greater detail than more distant, spatially unresolved galaxies.¹ For example, in typical ground-based optical imaging, galaxies with isophotal diameters larger than $\approx 10'' - 20''$ can be used to study the properties of their disk and spheroidal components as separate, distinct features; to identify bars, rings, disk asymmetries, and other dynamical structures; to discover and characterize their low surface-brightness features such as stellar streams, tidal tails, and outer envelopes; to unveil faint, low-mass satellites; and much more.

Because of their unique and high-impact scientific potential, compilations or atlases of large, nearby galaxies have a long, rich heritage in astronomy. In 1774, nearly 150

¹ We differentiate here between dwarf galaxies in the Local Group whose individual *stars* can be resolved (Mateo 1998), and galaxies which are near or large enough to be spatially resolved into *components* (e.g., bulge vs disk) but which must still be studied via their integrated light.



Figure 1. Optical mosaics of 42 galaxies from the SGA-2020 sorted by increasing angular diameter from the top-left to the bottom-right. Galaxies are chosen randomly from a uniform (flat) probability distribution in angular diameter. The horizontal white bar in the lower-left corner of each panel represents $1'$ and the mosaic cutouts range from $3\frac{1}{2}$ to $13\frac{1}{4}$. This figure illustrates the tremendous range of galaxy types, sizes, colors and surface brightness profiles, internal structure, and environments of the galaxies in the SGA.

years before observations confirmed that the Milky Way Galaxy was just one of many “island universes”, Charles Messier published his *Catalogue des Nébuleuses et des Amas d’Étoiles*, which includes 40 (now-famous) galaxies among a full catalog of 110 objects. Subsequently, building on the naked-eye surveying effort of William Herschel and his sister Caroline and son John (Herschel 1786, 1864), John Louis Emil Dreyer spent more than two decades assembling the *New General Catalogue of Nebulae and Clusters of Stars* (NGC) and the *Index Catalogues* (IC), a sample of approximately 15,000 Galactic and extragalactic objects whose designations are still in wide-spread use today (Dreyer 1888, 1912). The NGC, IC, and other early catalogs laid the foundation for several important galaxy atlases published in the second half of the 20th century covering most of the sky. These atlases used photographic imaging from the Palomar Observatory Sky Survey (POSS) in the 1950s and 1960s (Minkowski &

Abell 1963; Reid & Djorgovski 1993) and the UK Schmidt Southern Sky Survey in the 1970s (Cannon 1979), and include: the Catalogue of Galaxies and of Clusters of Galaxies (CGCG; Zwicky et al. 1968); the Uppsala General Catalog of Galaxies and its Addendum (UGC, UGCA; Nilson 1973, 1974); the Morphological Catalog of Galaxies (MCG; Vorontsov-Velyaminov & Krasnogorskaya 1974); the ESO/Uppsala Survey of the ESO (B) Atlas (ESO; Lauberts 1982); the Principal Galaxies Catalogue (PGC; Paturel et al. 1989); among others. Eventually, data from these and other catalogs were assembled into the indispensable Third Reference Catalog of Bright Galaxies (RC3; de Vaucouleurs et al. 1991; Corwin et al. 1994). The RC3 contains extensive information on 23,011 nearby galaxies and is purportedly complete for galaxies with $B_{t,\text{Vega}} < 15.5$, $D(25) > 1$ arcmin, and $v < 15,000$ km s $^{-1}$ ($z < 5 \times 10^{-5}$), although it does include a number of objects outside these limits which are of special interest.²

The advent of wide-area ($> 10^3$ deg 2), multi-wavelength imaging surveys have produced the next-generation atlases of large angular-diameter galaxies in the ultraviolet and infrared, including the 2MASS Large Galaxy Atlas (Jarrett et al. 2003), the NASA–Sloan Atlas (NSA; Blanton et al. 2005, 2011), the GALEX Ultraviolet Atlas of Nearby Galaxies (Gil de Paz et al. 2007), the Spitzer Survey of Stellar Structure in Galaxies (S 4 G; Sheth et al. 2010), the $z = 0$ Multiwavelength Galaxy Synthesis (z OMGS; Leroy et al. 2019), and the WISE Extended Source Catalog of the 100 Largest Galaxies (Jarrett et al. 2019). However, with the exception of the NSA, the optical sizes, shapes, and total magnitudes for the objects in these atlases are based on the photographic-plate measurements published in the RC3. The NSA, meanwhile, delivers new optical measurements of nearby ($z < 0.05$) galaxies using $\approx 8,000$ deg 2 of *ugriz* imaging from the Sloan Digital Sky Survey (SDSS; York et al. 2000), but is $\gtrsim 30\%$ incomplete at $r \lesssim 14$ (Wake et al. 2017).³

1.2. *The Need for a New Large-Galaxy Atlas*

With the historical context in mind, several recent developments motivate a renewed effort to assemble a uniform dataset of large angular-diameter galaxies. First, three new ground-based optical imaging surveys jointly called the DESI Legacy Imaging Surveys (hereafter, the Legacy Surveys) have delivered deep imaging in *g*, *r*, and *z* over $\approx 20,000$ deg 2 of the extragalactic (i.e., low Galactic extinction) sky (Dey et al. 2019; Schlegel et al. 2023, in prep.). These data provide exquisite photometric and astrometric precision and reach 1–2 magnitudes deeper than either SDSS or Pan-STARRS1 (Chambers et al. 2016). In addition, the development of the state-of-the-art image modeling code **The Tractor** provides a computationally tractable means of working with multi-band, multi-pass, variable-seeing imaging, enabling dedicated

² $D(25)$ represents the diameter of the galaxy at the 25 mag arcsec $^{-2}$ isophote in the optical and is a well-established and historically important measure of the “size” of a galaxy popularized by the RC3.

³ Fukugita et al. (2007) estimate the SDSS Main Survey (Strauss et al. 2002) to be $\gtrsim 50\%$ incomplete for $r \lesssim 14$ galaxies due to photometric shredding, which impacts other SDSS model galaxy catalogs (e.g., Simard et al. 2011; Meert et al. 2015). The NSA mitigates this incompleteness to some degree by utilizing redshifts from other surveys, but a non-negligible fraction of the largest, brightest galaxies in the local universe are still missed.

studies of large angular-diameter galaxies (Lang et al. 2016; Lang et al. 2023, in prep.).

Second, in May 2021 the Dark Energy Spectroscopic Instrument (DESI) Survey began a five-year program (2021–2026) to obtain precise spectroscopic redshifts for an unprecedented sample of more than 40 million galaxies and 10 million stars over the $\approx 14,000 \text{ deg}^2$ Legacy Surveys footprint accessible from the 4-meter Mayall Telescope at Kitt Peak National Observatory (DESI Collaboration et al. 2016a,b; Abareshi et al. 2022). As part of this effort, the DESI Bright Galaxy Survey (BGS) is obtaining spectra and redshifts for a statistically complete sample of > 10 million galaxies brighter than $r = 20.175$ (Hahn et al. 2023). A high-quality photometric catalog of the largest angular-diameter galaxies over the DESI footprint is needed to ensure the BGS has high completeness and does not suffer from the photometric shredding and spectroscopic incompleteness of the SDSS at bright magnitudes (Fukugita et al. 2007; Wake et al. 2017).

To address these and other needs, we present the 2020 version of the Siena Galaxy Atlas (SGA), SGA-2020, an optical and infrared imaging atlas of nearly 4×10^5 galaxies approximately limited to an angular diameter of $25''$ at the $26 \text{ mag arcsec}^{-2}$ isophote for galaxies brighter than $r \approx 18$ over the $20,000 \text{ deg}^2$ footprint of the DESI Legacy Imaging Surveys Data Release 9 (LS/DR9; Dey et al. 2019; Schlegel et al. 2023, in prep.; see Figure 1). The SGA-2020 delivers precise coordinates, multi-wavelength mosaics, azimuthally averaged optical surface brightness and color profiles, model images and photometry, and additional metadata for the full sample.⁴ Notably, for many of the largest (e.g., NGC/IC/Messier) galaxies in the sky, especially outside the SDSS imaging footprint, the SGA-2020 delivers the first reliable measurements of the optical positions, shapes, and sizes of large galaxies since the RC3 was published more than 30 years ago.

By combining existing (archival) spectroscopic redshifts with forthcoming DESI spectroscopy, the SGA-2020 will spur a renewed effort to tackle several outstanding problems in extragalactic astrophysics, particularly the interplay between galaxy formation and dark matter halo assembly. It will also support studies of time-domain and multi-messenger astronomical events, which are often hampered by incomplete or heterogeneous catalogs of large, nearby galaxies which are most likely to host the electromagnetic counterparts of gravitational wave events (Gehrels et al. 2016; Abbott et al. 2020) and other classes of transients. Moreover, within the $\approx 14,000 \text{ deg}^2$ DESI footprint, the SGA-2020 is ensuring high photometric completeness for the BGS, and is facilitating high-impact ancillary science through a variety of secondary targeting programs (Myers et al. 2023; DESI Collaboration et al. 2023a). For example, the DESI Peculiar Velocity Survey will place precise new constraints on the growth rate of large-scale structure by measuring the Tully–Fisher and Fundamental-Plane

⁴ <https://sga.legacysurvey.org>

scaling relations (Tully & Fisher 1977; Djorgovski & Davis 1987) from SGA-2020 targets at $z < 0.15$ (Saulder et al. 2023). And finally, the SGA-2020 will help engage the broader public with visually striking color mosaics of large, well-resolved, nearby galaxies, enabling a myriad of educational and public-outreach activities.

We organize the remainder of the paper in the following way: In §2 we define the SGA-2020 parent sample and describe the procedure we use to define the final sample of galaxies and their associated (angular) group membership. In §3, we describe our photometric analysis, including how we construct the custom multi-wavelength mosaics, model the two-dimensional images of each galaxy, and measure their azimuthally averaged surface-brightness and color profiles. Of particular interest for some readers may be §3.3, where we validate our surface-brightness profiles and summarize the principal SGA-2020 data products. In §4, we quantify the completeness of the SGA and review how it improves upon existing large-galaxy catalogs, and in §5 we highlight some of the exciting potential scientific applications of the SGA-2020. Finally, §6 summarizes the main results of this paper and outlines some of the improvements we intend to include in the next version of the Siena Galaxy Atlas.

Note that unless otherwise indicated, all magnitudes are on the AB magnitude system (Oke & Schild 1970) and have not been corrected for foreground Galactic extinction. We report all fluxes in units of “nanomaggies”, where 1 nanomaggie is the (linear) flux density of an object with an AB magnitude of 22.5.⁵

2. PARENT SAMPLE & GROUP CATALOG

2.1. *Building the Parent Sample*

Many of the largest, highest surface-brightness galaxies in the sky have been famously known for a long time and are part of many of the legacy (photographic-plate) large-galaxy catalogs discussed in §1 (e.g., RC3). More recently, fainter, lower surface-brightness (but still “large”, spatially resolved) galaxies have been cataloged by modern, wide-area optical and near-infrared imaging surveys like the SDSS, the Two Micron All Sky Survey (2MASS; Skrutskie et al. 2006), and Pan-STARRS1 (Chambers et al. 2016). For the first version of the Siena Galaxy Atlas, we opt to build upon this body of previous work by beginning from these and other catalogs of “known” large angular-diameter galaxies (but see the discussion in §6).

Fortunately, several user-oriented databases exist which curate the positions, sizes, magnitudes, redshifts, and other information on millions of extragalactic sources cataloged by different surveys, including SIMBAD (Wenger et al. 2000), the NASA Extragalactic Database (NED; Helou et al. 1991), and HyperLeda (Makarov et al. 2014). After some experimentation, we opt to construct the initial SGA-2020 parent sample using the HyperLeda⁶ extragalactic database. HyperLeda includes extensive metadata on nearly all known large angular-diameter galaxies, building on the her-

⁵ <https://www.legacysurvey.org/dr9/description/#photometry>

⁶ <http://leda.univ-lyon1.fr/>

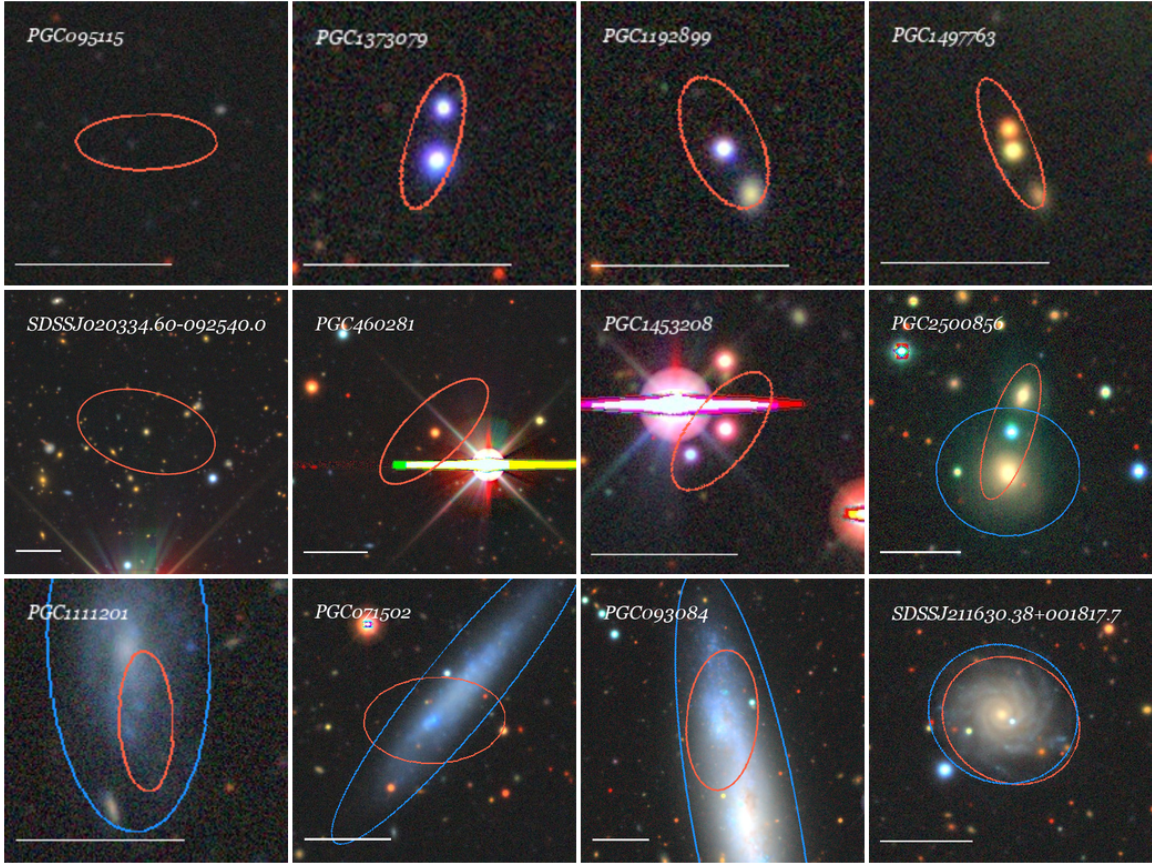


Figure 2. Gallery of common types of HyperLeda sources rejected while building the parent sample. In each panel the horizontal white bar represents $30''$. The top row shows one spurious object and three examples of pairs or triples of stars or compact galaxies which are recorded in HyperLeda as one “large” galaxy (represented by the *red ellipse*). The middle row shows four examples of how bright stars and galaxies can lead to significantly over-estimated galaxy diameters in HyperLeda. For example, PGC2500856 in the middle-right panel is a blue star which has been miscategorized by HyperLeda as a galaxy with a major-axis diameter of $\approx 54''$ presumably due to the proximity of the nearby bright galaxy PGC3087062 which appears in the final SGA-2020 catalog (*blue ellipse*). Finally, the bottom row shows four examples of sources in HyperLeda which are in fact photometric shreds or misidentified parts of a galaxy. In each case, the blue ellipse shows the correct parent galaxy from the SGA-2020 while the red ellipse is the incorrect source from HyperLeda which we remove from the parent sample (see §2.1). For example, PGC071502 and PGC093084 are H II regions in ESO240-004 and NGC1507, respectively, while SDSSJ211630.38+001817.7 is a foreground star in the body of PGC188224 with an incorrect angular diameter.

itage of the RC3 and earlier large-galaxy atlases. In addition, an effort has been made by the HyperLeda team to *homogenize* the angular diameters, magnitudes, and other observed properties of the galaxies which have been ingested into the database from a wide range of different surveys and catalogs (Paturel et al. 1997; Makarov et al. 2014). This procedure imposes some uniformity on our parent sample, although we show in §3.3 the significant value of computing the geometry (diameter, position angle, and ellipticity) and photometry of galaxies consistently and using modern (deep, wide-area) optical imaging.

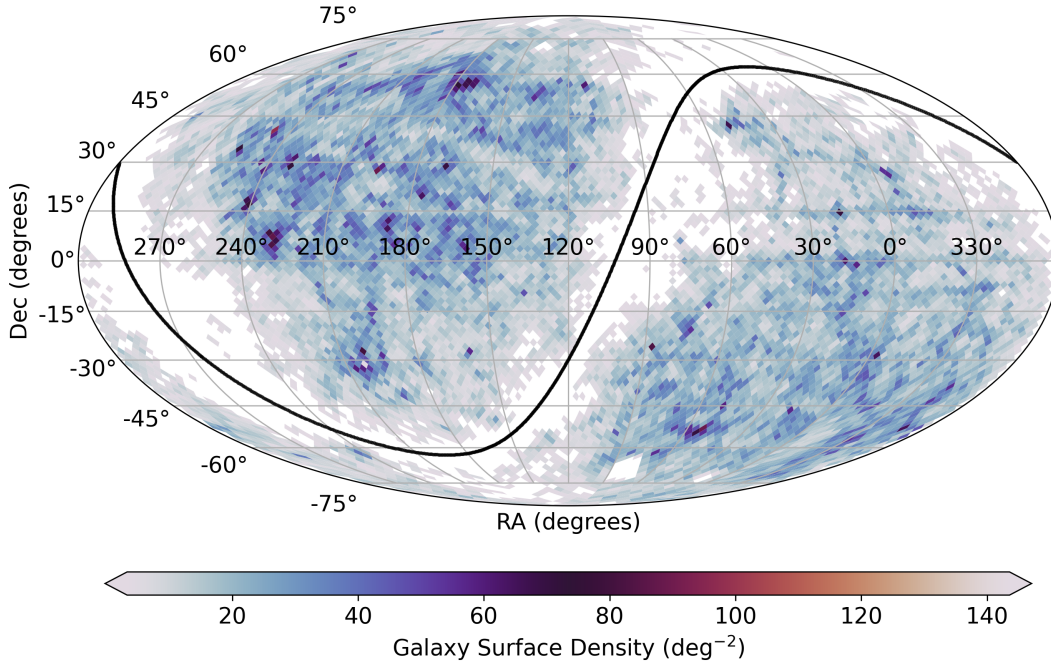


Figure 3. Distribution of 531,677 galaxies in the SGA-2020 parent sample in an equal-area Mollweide projection in equatorial coordinates, binned into 3.4 deg^2 healpix pixels (Zonca et al. 2019). The dark gray curve represents the Galactic plane. Note the significant variations in galaxy surface density, which we attribute to surface-brightness incompleteness and heterogeneity in the aggregate HyperLeda catalog.

With these ideas in mind, we query the HyperLeda extragalactic database for galaxies with angular diameter $D_L(25) > 12''$ ($0'.2$), where $D_L(25)$ is the major-axis diameter of the galaxy at the $25 \text{ mag arcsec}^{-2}$ surface brightness isophote in the optical (typically the Johnson–Morgan B -band; see Appendix A for additional details). Our query results in an initial parent sample of 1,436,176 galaxies.

Using visual inspection and a variety of quantitative and qualitative tests, we cull this initial sample by applying the following additional cuts: First, we remove the Large and Small Magellanic Clouds and the Sagittarius Dwarf Galaxy from the sample by imposing a maximum angular diameter of $D_L(25) < 180'$. These galaxies span such a large projected angular size on the sky (many degrees) that their inclusion is outside the scope of the Siena Galaxy Atlas (but see Jarrett et al. 2019). After removing these objects, the largest angular-diameter galaxies which remain are NGC0224=M31 and NGC0598=M33 whose $D_L(25)$ diameters are $178'$ and $62'$, respectively.

Furthermore, we limit the sample on the lower end to $D_L(25) > 20''$, which removes roughly 900,000 galaxies (approximately 65% of the initial sample). We implement this cut because we find that the fraction of sources with incorrect (usually over-estimated) diameters in HyperLeda increases rapidly below this limit. Moreover, we

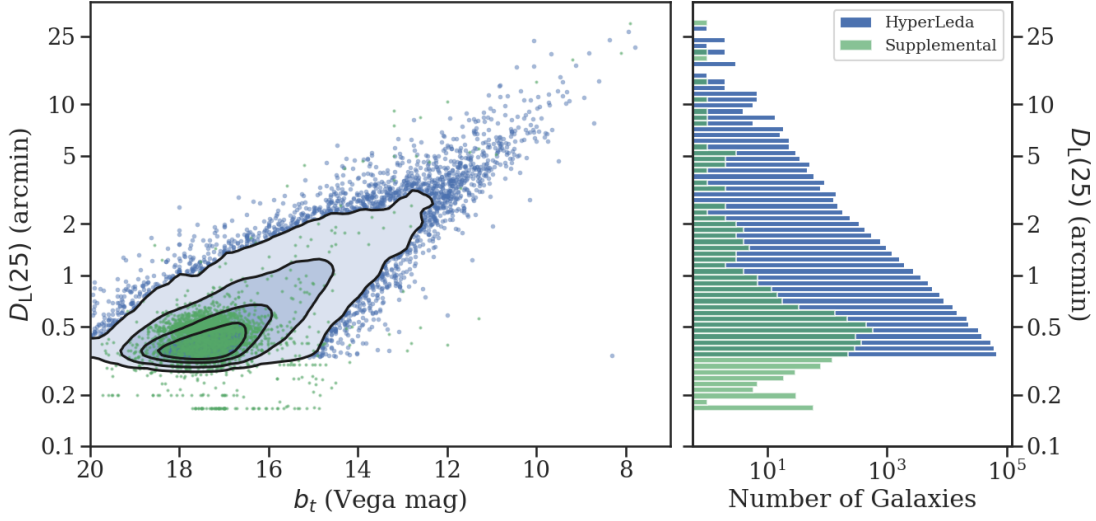


Figure 4. Isophotal diameter, $D_L(25)$, versus b_t -band magnitude (*left*) and marginalized distribution of $D_L(25)$ (*right*) for the SGA-2020 parent sample. The blue contours, points, and histogram represent galaxies from HyperLeda, while the green points and histogram are galaxies from the supplemental catalogs we use to increase the completeness of the sample (see §2.1). For reference, the contours enclose 50%, 75%, 95%, and 99.5% of the blue points. These figures show that, by construction, the SGA-2020 parent sample is largely limited to $D_L(25) > 20''$ ($0'.333$) but with a tail of galaxies with diameters as small as $\approx 10''$ ($\approx 0'.167$), and it includes galaxies as bright as $b_{t,\text{Vega}} \approx 8$.

find that galaxies smaller than $D_L(25) \approx 20''$ are well-modeled by **Tractor** as part of the standard photometric pipeline used in LS/DR9 (Dey et al. 2019; Schlegel et al. 2023, in prep.).

Next, we remove approximately 3800 galaxies with no magnitude estimate in HyperLeda (as selected by our query; see Appendix A), which we find to be largely spurious, as well as approximately 6500 objects with significantly overestimated diameters (or spurious sources) which we identify via visual inspection. Many of these cases are groupings of small galaxies or stars along a line which have been misinterpreted by previous fitting algorithms as a single edge-on galaxy. In addition, we remove approximately 1700 galaxies whose primary galaxy identifier (in HyperLeda) is from either SDSS or 2MASS and whose central coordinates place it inside the elliptical aperture of another (non-SDSS and non-2MASS) galaxy with $D_L(25)$ diameter greater than $30''$. We find that in the majority of cases these objects have grossly over-estimated diameters, presumably due to shredding by the 2MASS and SDSS photometric pipelines. Figure 2 displays a gallery of some of the most common types of sources we reject from our initial parent sample using these cuts.

Now, to improve the completeness of the parent sample, we supplement the initial HyperLeda catalog with sources drawn from three additional catalogs, making sure to carefully handle duplicate entries. First, we add a subset of the Local Group dwarf galaxies from McConnachie (2012). From the original sample of 93 galaxies

in [McConnachie \(2012\)](#), we remove 47 which have such a low surface-brightness and are so well-resolved that including them is beyond the scope of the current version of the Siena Galaxy Atlas.⁷ For reference, the median surface-brightness of these 47 systems is $\mu_V = 28.8 \text{ mag arcsec}^{-2}$, well below the surface-brightness completeness limit of the SGA-2020 (see §3.3). Furthermore, we remove the Fornax and Sculptor dwarf galaxies, which are higher surface-brightness ($\mu_V = 25.1 - 25.5 \text{ mag arcsec}^{-2}$) but very well-resolved into stars and star clusters and too challenging to include in this initial version of the SGA.

Next, we add 190 galaxies from the RC3 and OpenNGC⁸ catalogs which are missing from our initial HyperLeda sample. Surprisingly, many of these systems are large and have high average surface brightness; however, we suspect that an issue with our database query (see Appendix A) may have inadvertently excluded these sources from our initial catalog. And finally, we use the Legacy Surveys Data Release 8 (DR8) photometric catalogs to identify 2890 additional large-diameter galaxies in the Legacy Surveys footprint.⁹ Specifically, after applying a variety of catalog-level quality cuts and extensive visual inspection, we include in our parent sample all objects (not already in our sample) from DR8 with half-light radii $r_{50} > 14''$ based on their Tractor model fits.

Our final parent sample contains 531,677 galaxies approximately limited to $D_L(25) > 20''$ and spanning a wide range of magnitude and surface brightness. In Figure 3 we show the celestial distribution of this sample and in Figure 4 we show the range of apparent b_t -band magnitude¹⁰ and angular diameter spanned by the parent sample. We discuss the completeness of the sample in §4.

2.2. Projected Group Catalog

Our approach for the Siena Galaxy Atlas is to jointly analyze galaxies which are relatively close to one another in terms of their projected (or angular) separation in order to properly fit overlapping light profiles. We emphasize that we do not require galaxies to be *physically* associated, which would require knowledge of their redshifts or physical separation. We build a simple group catalog from the parent sample described in §2.1 using the *sphergroup* friends-of-friends algorithm.¹¹ We use a 10' linking length, taking care to ensure that galaxies assigned to the same group overlap within two times their circularized $D_L(25)$ diameter.

Using this procedure, we identify 14,930 projected galaxy groups with two members, 1585 groups with 3–5 members, 51 with 6–10 members, and just four groups with more than 10 members, including the center of the Coma Cluster, the Virgo Cluster, and Abell 3558 (although Abell 3558 is outside the LS/DR9 imaging footprint; see

⁷ For reference, we remove the following Local Group dwarfs: Andromeda I, II, III, V, VII, IX, X, XI, XII, XIII, XIV, XV, XVI, XVII, XVIII, XIX, XX, XXI, XXII, XXIII, XXIV, XXV, XXVI, XXVII, and XXIX; Antlia; Aquarius; Bootes I and II; Canes Venatici I and II; Carina; Coma Berenices; Draco; Hercules; Leo IV, V, and T; Pisces II; Sagittarius dSph; Segue I and II; Sextans I; Ursa Major I and II; Ursa Minor; and Willman 1.

⁸ <https://github.com/mattiaverga/OpenNGC>

⁹ <https://www.legacysurvey.org/dr8>

¹⁰ <http://leda.univ-lyon1.fr/leda/param/bt.html>

¹¹ <https://pydl.readthedocs.io/en/latest>

§3.3). Notably, 496,255 objects or 93% of the parent sample, are isolated according to the criteria used to build the group catalog.

For each galaxy group, we compute several quantities which we refer to in subsequent sections of the paper (but see Appendix B for the complete data model). `GROUP_NAME` is a unique group name, which we construct from the name of the group’s largest member (ranked by $D_L(25)$) and the suffix `_GROUP` (e.g., `NGC4406_GROUP`). For isolated galaxies, `GROUP_NAME` is just the name of its only member (i.e., without the `_GROUP` suffix). In addition, we compute `GROUP_RA` and `GROUP_DEC` to be the $D_L(25)$ -weighted right ascension and declination, respectively, of all the group members. Once again, for isolated systems, `GROUP_RA` and `GROUP_DEC` are identical to the RA and DEC coordinates of that galaxy (see Appendix B). Finally, we record our estimate of the diameter of the group in the quantity `GROUP_DIAMETER`. For isolated galaxies, `GROUP_DIAMETER` equals $D_L(25)$, but for groups we compute `GROUP_DIAMETER` to be the maximum separation of all the pairs of group members plus their $D_L(25)$ diameter (in arcmin).

3. PHOTOMETRIC ANALYSIS

3.1. *Imaging Data*

We build the SGA-2020 from the same optical and infrared imaging data used to produce the Legacy Surveys DR9 (Dey et al. 2019; Schlegel et al. 2023, in prep.).¹² Briefly, the optical data consist of *grz* imaging over $\approx 20,000$ deg² from a number of different surveys. In the North Galactic Cap (NGC), we use data from the Beijing–Arizona Sky Survey (BASS; Zou et al. 2017), which provides $\approx 5,000$ deg² of *gr* imaging using the 90Prime Camera (Williams et al. 2004) on the Steward Observatory Bok 2.3-meter telescope at Kitt Peak National Observatory (KPNO); and data from the Mayall *z*-band Legacy Survey (MzLS), which provides *z*-band imaging over the same $\approx 5,000$ deg² footprint as BASS using the Mosaic-3 camera (Dey et al. 2016) at the KPNO Mayall 4-meter telescope.

In the South Galactic Cap (SGC) and in the NGC up to a declination of approximately $+32^\circ$, we use *grz* imaging over $\approx 15,000$ deg² from roughly 50 distinct (but uniformly processed) datasets obtained with the Dark Energy Camera (DECam; Flaugher et al. 2015) at the Cerro Tololo Inter-American Observatory (CTIO) 4-meter Blanco telescope. Note that the majority of this DECam imaging comes from the DECam Legacy Survey (DECaLS; Dey et al. 2019) and the Dark Energy Survey (DES; Dark Energy Survey Collaboration et al. 2016; Abbott et al. 2021).¹³

We supplement the optical data with all-sky infrared imaging at $3.4 - 22$ μm from the Wide-Field Infrared Survey Explorer (WISE; Wright et al. 2010). Specifically, we use the 6-year WISE plus NEOWISE-Reactivation (NEOWISE-R; Mainzer et al. 2014) image stacks in W1 (3.4 μm) and W2 (4.6 μm) from Meisner et al. (2021),

¹² <https://www.legacysurvey.org/dr9>

¹³ See Dey et al. (2019) for a complete list of the DECam programs used.

and the W3 (12 μm) and W4 (22 μm) unblurred image stacks from Lang (2014); collectively, we refer to these custom image stacks as the unWISE coadds.¹⁴ Note that in the SGA-2020 we produce WISE image coadds for each galaxy (or galaxy group) in the sample but do not measure the infrared surface-brightness profiles; however, we intend to deliver the infrared (and ultraviolet) surface-brightness profiles and integrated photometry in a future version of the Siena Galaxy Atlas (see §6).

3.2. Multi-Wavelength Mosaics & Surface Brightness Profiles

At this point in the analysis we have multiband optical and infrared imaging covering roughly half the sky (§3.1) and an input parent catalog of central coordinates and system diameters for more than half a million sources (§2.2). The next steps are to build custom multi-wavelength mosaics centered on each of these positions (§3.2.1); model all the sources in the field using **The Tractor** (§3.2.2); and measure elliptical aperture photometry and azimuthally averaged surface-brightness profiles (§3.2.3).

Before proceeding, we briefly summarize the principal software products we use, as well as the relationship between them. First, given an astrometrically and photometrically calibrated image, inverse variance image, and knowledge of the point-spread function (PSF), **The Tractor**¹⁵ uses the PSF and a family of two-dimensional galaxy models to forward-model the observed pixel-level data (Lang et al. 2016; Dey et al. 2019; Lang et al. 2023, in prep.). One of the principal advantages of **The Tractor** is that it handles multi-band, multi-CCD, variable-PSF imaging in a statistically rigorous way, which is especially important when dealing with the full range of optical and infrared (WISE) data from the Legacy Surveys. In order to handle the imaging data, the Legacy Surveys team has developed **legacypipe**¹⁶, a photometric pipeline which wraps **The Tractor** as its fitting engine and conveniently handles many tasks related to this imaging dataset (Dey et al. 2019). Finally, for the Siena Galaxy Atlas project specifically, we have developed the **SGA**¹⁷ and **legacyhalos**¹⁸ software products, which rely on some of the lower-level **legacypipe** functionality (with MPI-parallelization) but also include code to carry out the non-parametric photometric analysis which is one of the cornerstone data products of the SGA-2020 (see §3.3).

3.2.1. Mosaics

Given the diameter of each system and its central coordinates (GROUP_RA, GROUP_DEC, and GROUP_DIAMETER; see §2.2), we first determine if LS/DR9 imaging exists in all three *grz* bands over at least 90% of the area. If not, we remove that system from further analysis (including, unfortunately, NGC0224=M31, where we only have MzLS *z*-band imaging). Then, for the remaining objects, we generate *g*-, *r*-, and *z*-band mosaics with a size which depends on the group size: for groups with

¹⁴ <http://unwise.me>

¹⁵ <https://github.com/dstndstn/tractor>

¹⁶ <https://github.com/legacysurvey/legacypipe>

¹⁷ <https://github.com/moustakas/SGA>

¹⁸ <https://github.com/moustakas/legacyhalos>

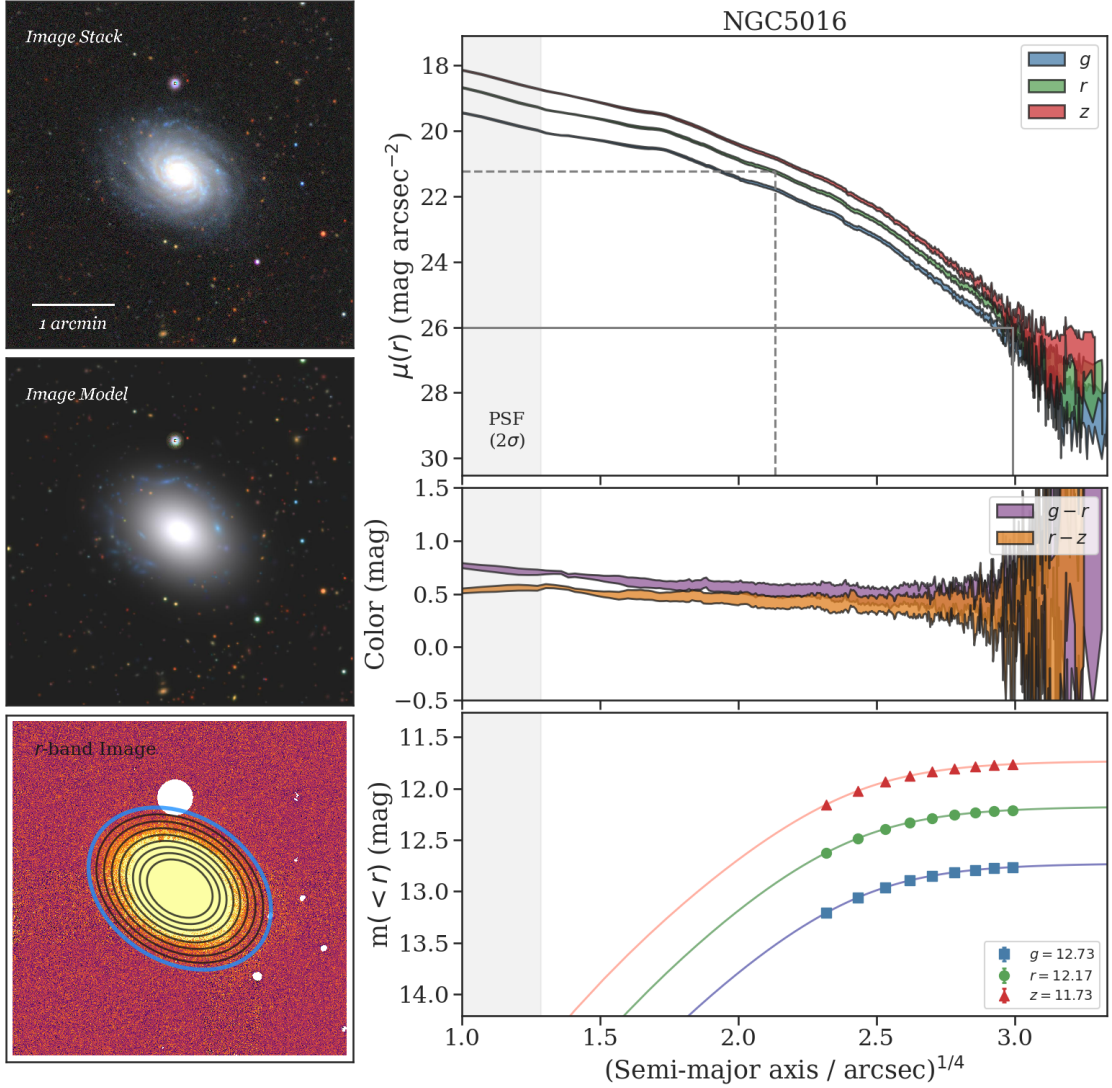


Figure 5. Illustration of the key steps and data products of the SGA-2020 pipeline for one example galaxy, NGC5016. The three panels on the left-hand side show (*top-left*) a color montage of the optical imaging; (*middle-left*) a color montage of the corresponding **Tractor** model image; and (*bottom-left*) the *r*-band image with masked pixels zeroed out (*white pixel values*). The nested black ellipses in this panel correspond to nine surface-brightness levels between $\mu_r = 22$ and 26 mag arcsec $^{-2}$ in 0.5 mag arcsec $^{-2}$ steps, with the solid blue isophote representing the outermost, $R(26)$, size of the galaxy. The right-hand panels show (*top-right*) the azimuthally averaged *g*- (*blue*), *r*- (*green*), and *z*-band (*red*) surface-brightness profiles as a function of the semi-major axis; (*middle-right*) the observed-frame $g - r$ (*purple*) and $r - z$ (*orange*) color profiles; and (*bottom-right*) the apparent brightness of NGC5016 in *g* (*filled blue squares*), *r* (*filled green circles*), and *z* (*filled red triangles*) measured within the same elliptical apertures shown in the lower-left panel. The dashed- and solid-gray lines in the top-right panel indicate, for reference, the *r*-band half-light radius from equation (2) and the $R(26)$ radius, respectively, and the bottom-right panel also shows the best-fitting curve-of-growth models (independently fit to the photometric data in each bandpass) given by equation (1). The legend in the lower-right panel also provides the integrated (asymptotic) *grz* magnitudes for this galaxy.

$\text{GROUP_DIAMETER} < 14'$ we generate a mosaic of diameter $3 \times \text{GROUP_DIAMETER}$; for groups with $14' < \text{GROUP_DIAMETER} < 30'$ we generate a mosaic of diameter $2 \times \text{GROUP_DIAMETER}$; and for NGC0598=M33, whose GROUP_DIAMETER is $> 30'$, we use a mosaic diameter of $1.4 \times \text{GROUP_DIAMETER}$. We also choose the input imaging according to the following criteria: We use the DECam imaging (from DECaLS and DES) for all of the South Galactic Cap, and for the North Galactic Cap when $\text{GROUP_DEC} < 32:375$; and the BASS plus MzLS imaging otherwise (see §4.1.3 of Myers et al. 2023).

Our analysis begins with reduced and calibrated CCD-level 90Prime, Mosaic-3, and DECam imaging. These reduced data are generated using the NOIRLab Community Pipeline (CP) dedicated to each instrument (e.g., Valdes et al. 2014), together with several custom data-reduction steps developed by the Legacy Surveys team. We refer the reader to Dey et al. (2019) and Schlegel et al. (2023, in prep.) for a detailed description of these data-reduction procedures. Briefly, we use Pan-STARRS1 PSF photometry (Chambers et al. 2016; Finkbeiner et al. 2016) transformed to the natural filter system of each instrument for photometric calibration¹⁹ and Gaia Data Release 2 (Gaia Collaboration et al. 2018) stellar positions for astrometry²⁰. The average photometric precision for bright (but unsaturated) stars is better than ± 10 mmag in grz over the full footprint, and the astrometric precision is approximately $\pm 0''.030$ for DECam and Mosaic-3 and $\pm 0''.12$ mas for 90Prime (Dey et al. 2019).

Accurate large-galaxy photometry depends crucially on robust and unbiased background-subtraction. For the SGA-2020, we utilize the same background-subtracted images used for LS/DR9. As we discuss below and in §3.3, however, the sky-subtracted data do contain systematic errors which we intend to mitigate in future versions of the SGA (see the discussion in §6).

First, the CP carefully masks astrophysical sources and then subtracts the large-scale sky-pattern across the field of view from each exposure using a low-order spline model derived from robust statistics measured on the individual CCDs. We note that the 90Prime, Mosaic-3, and DECam CCDs are approximately $30' \times 30'$, $17'.5 \times 17'.5$, and $9' \times 18'$, respectively, so the angular scale of this background model is much larger than all but the largest galaxies in the SGA-2020. Next, the CP subtracts the camera reflection pattern (or pupil ghost) from the DECam and Mosaic-3 data and the fringe pattern from the Mosaic-3 z -band and 90Prime r -band data. Telescope reflections from very bright stars are not removed. Next, the CP aggressively subtracts the high-frequency pattern noise (caused by a drifting amplifier bias level) present in the Mosaic-3 imaging. The pattern fitting was designed to preserve counts in smaller galaxies and stars but, unfortunately, has a significant effect on the low surface-brightness, outer envelopes of the galaxies in our sample. This pattern-noise subtraction affects all the MzLS imaging and causes galaxies to appear *too green* in

¹⁹ <https://www.legacysurvey.org/dr9/description/#photometry>

²⁰ <https://www.legacysurvey.org/dr9/description/#astrometry>

the *grz* color mosaics (see Appendix C). For DECam, we also subtract a residual *g*-, *r*-, and *z*-band sky pattern and a *z*-band fringe pattern from the data using median-scaled templates derived from multiple exposures (in a given bandpass) within one or more nights.²¹ Finally, we remove the spatially varying sky-background on the smallest scales by dividing each CCD into 512-pixel boxes, computing the robust median, and using spline interpolation to build the final background map. During this step, we mask pixels which lie within the elliptical aperture of any galaxy in the SGA-2020 parent catalog (from §2.1), as well as Gaia stars and other sources detected in each image.

Finally, with all the reduced data in-hand, we build the full-field mosaic for each galaxy (or galaxy group) as the inverse-variance weighted sum of all the available imaging (in each bandpass) projected onto a tangent plane using Lanczos-3 (sinc) resampling. For the *grz* imaging we adopt a constant pixel scale of $0''.262 \text{ pixel}^{-1}$ and for the unWISE mosaics we use $2''.75 \text{ pixel}^{-1}$. The left panels of Figures 5 and 6 show, as examples, the *grz* color mosaics for the isolated galaxy NGC5016 and PGC193192, a member of the PGC193199 Group, respectively.

3.2.2. *Tractor* Modeling & Masking

We use **The Tractor** to model all the sources in a given mosaic, including the large angular-diameter galaxies of interest. Note that all source detection and model fitting with **The Tractor** takes place on these coadded images (triggered by invoking the `--fit-on-coadds` option in `legacypipe`), unlike for the standard DR9 processing in which all model fitting is done using the unresampled CCD images jointly (see Dey et al. 2019 and Schlegel et al. 2023, in prep.).

Before fitting, we multiply the optical inverse variance mosaics (*iv*) by a factor of $\sqrt{iv/iv_{50}}$, where iv_{50} is the median inverse variance of the mosaic. This rescaling down-weights the bright central regions of galaxies even more than they already are from source Poisson noise and has the practical effect of mitigating the tendency of **The Tractor** to fit the high-surface brightness central region of each galaxy at the expense of its outer envelope. In addition, we increase the threshold for detecting and deblending sources by specifying `--saddle-fraction 0.2` and `--saddle-min 4.0` (the default values are 0.1 and 2.0, respectively). The `saddle-fraction` parameter controls the fractional peak height for identifying new sources around existing sources and `saddle-min` is the minimum required saddle-point depth (in units of the standard deviation of pixel values above the noise) from existing sources down to new sources. We find these options necessary in order to prevent excessive shredding and overfitting of the *resolved* galactic structure in individual galaxies (e.g., H II regions). Finally, **The Tractor** detects sources, creates a segmentation map, and then uses the mean PSF of the coadd to compute the two-dimensional, maximum-likelihood model of each source (fitting all three *grz* bands simultaneously) from among the following

²¹ <https://www.legacysurvey.org/dr9/sky>

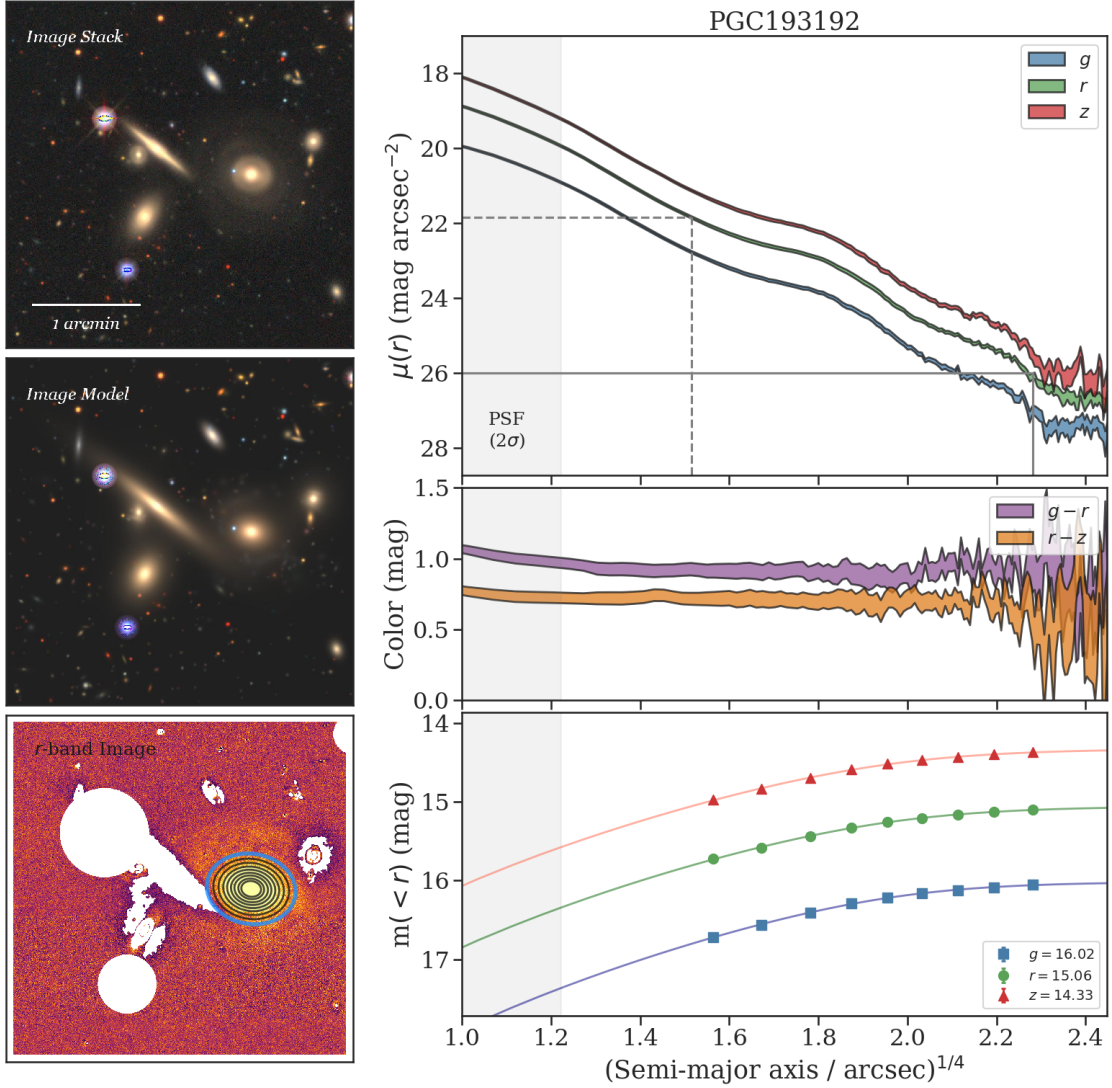


Figure 6. Like Figure 5, but for PGC193192, the second-largest member of the PGC193199 Group.

possibilities: PSF, REX, EXP, DEV, or SER.²² For reference, we construct the PSF of the coadd as the inverse-variance weighted average PSF of the individual pixelized PSFs contributing to the coadd, which is sufficient given that the galaxies we are interested in, $D_L(25) \gtrsim 20''$, are significantly larger than the optical image quality, $\text{PSF}_{\text{FWHM}} \approx 1'' - 2''$.

The middle-left panels of Figures 5 and 6 show The Tractor model image stack for NGC5016 and the PGC193199 Group, respectively. Overall, the model is an excellent description of the data, particularly for the small, compact sources in the field. However, note how The Tractor fits the (resolved) spiral arms in NGC5016

²² Briefly, REX is a round ($\epsilon = 0$) exponential galaxy model with variable half-light radius; EXP and DEV represent an exponential and de Vaucouleurs (1948) galaxy profile, respectively; and SER is a Sersic (1968) galaxy model (see Dey et al. 2019 and the LS/DR9 documentation for more details).

as elongated blue “galaxies”, and the extended outer envelopes of the early-type galaxy models in the PGC193199 Group compared to the data. Despite these issues, **The Tractor** models of the large galaxies in our sample are extremely useful and complementary to the non-parametric photometric measurements we carry out in §3.2.3.

Using **The Tractor** models, we next build an image mask which we use in §3.2.3. First, we read the `maskbits`²³ bit-mask image produced as part of the pipeline, but only retain the `BRIGHT`, `MEDIUM`, `CLUSTER`, `ALLMASK_G`, `ALLMASK_R`, and `ALLMASK_Z` bits. Hereafter, we refer to this mask as the `starmask`. Next, we build a `residual mask` which accounts for statistically significant differences between the data and the **Tractor** models. In detail, we flag all pixels which deviate by more than 5σ (in any bandpass) from the absolute value of the Gaussian-smoothed residual image, which we construct by subtracting the model image from the data and smoothing with a 2-pixel Gaussian kernel. This step obviously masks all sources, including the large galaxies of interest, but we restore those pixels in the next step. In addition, we iteratively dilate the mask two times and mask pixels along the border of the mosaic with a border equal to 2% the size of the mosaic.

Then, we iterate on each galaxy in the group from brightest to faintest based on **The Tractor** r -band flux and carry out the following steps: (1) For each galaxy, we construct the model image from all **Tractor** sources in the field *except* the galaxy of interest and subtract this model image from the data. (2) We measure the mean elliptical geometry of the galaxy (center, ellipticity, position angle, and approximate semi-major axis length) based on the second moment of the light distribution (hereafter, the `ellipse moments`) using a modified version of Michele Cappellari’s `mge.find_galaxy`²⁴ algorithm (Cappellari 2002). When computing the `ellipse moments`, we first median-filter the image with a 3-pixel boxcar to smooth out any small-scale galactic structure and we only use pixels with $\mu_r < 27 \text{ mag arcsec}^{-2}$. (3) Finally, we combine the `residual mask` with the `starmask` (using Boolean logic) but we unmask pixels belonging to the galaxy based on the `ellipse moments` geometry using 1.5 times the estimated semi-major axis of the galaxy.

Occasionally, the preceding algorithm fails in fields containing more than one galaxy if the central coordinates of one of the galaxies is masked by a previous (brighter) system. We consider a source to be impacted if any pixel in a 5×5 pixel box centered on **The Tractor** position of the galaxy is masked. In this case, we iteratively shrink the elliptical mask of any of the previous galaxies until the central position of the galaxy currently being analyzed is unmasked. We emphasize that this algorithm is not perfect, particularly in very crowded galactic fields like the center of the Coma Cluster, but we intend to improve it in future versions of the Siena Galaxy Atlas. Another occasional failure mode is if the flux-weighted position of the galaxy based on

²³ <https://www.legacysurvey.org/dr9/bitmasks/#maskbits>

²⁴ <http://www-astro.physics.ox.ac.uk/~mxc/software/#mge>

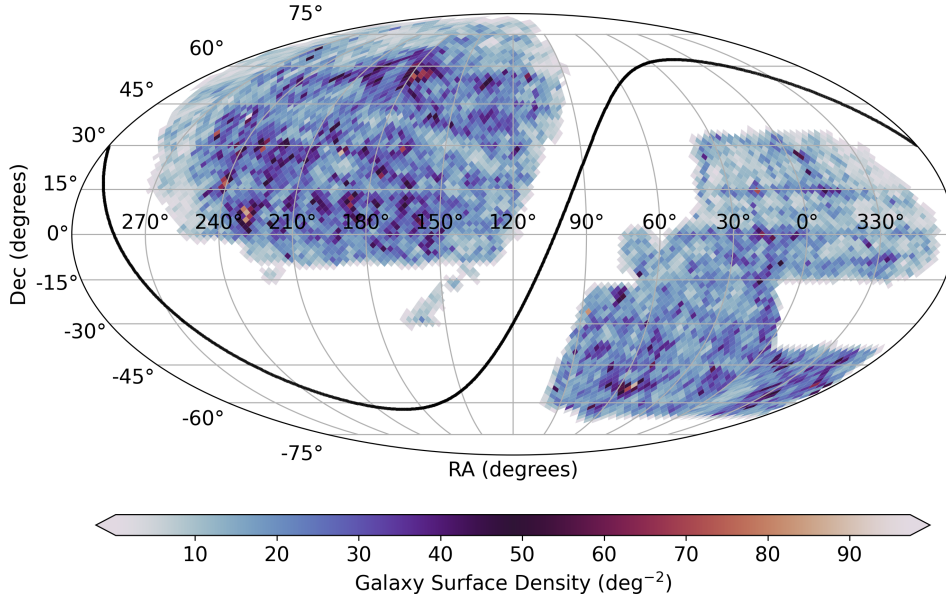


Figure 7. Distribution of 383,620 galaxies in the final SGA-2020 sample (to be compared with Figure 3 but note the different colorbar scales).

the `ellipse moments` differs by `The Tractor` position by more than 10 pixels, which can happen in crowded fields and near bright stars and unmasked image artifacts; in this case we revert to using `The Tractor` coordinates and model geometry.

The bottom-left panels of Figures 5 and 6 show the final masked r -band image for NGC5016 and PGC193192, respectively.

3.2.3. Surface-Brightness Profiles

With the multi-wavelength mosaics and per-galaxy image masks in-hand, we next measure the surface brightness profiles and photometric curves of growth for each galaxy in the sample using the standard ellipse-fitting and aperture photometry techniques in `photutils`²⁵ (Bradley 2023). We assume a fixed elliptical geometry as a function of semi-major axis using the `ellipse moments` measured in §3.2.2, and robustly determine the surface brightness along each elliptical path from the light-weighted central pixel to two times the estimated semi-major axis of the galaxy in a 1-pixel ($0''.262$) interval. In detail, we measure the surface brightness (and the uncertainty) using two sigma-clipping iterations, a 3σ clipping threshold, and median-area integration.²⁶

From the r -band surface brightness profile, we also robustly measure the size of the galaxy at nine equally spaced surface-brightness thresholds between $\mu_r = 22$ and

²⁵ <https://photutils.readthedocs.io/en/stable>

²⁶ In other words, we use `nclip=2`, `sclip=3`, and `integrmode=median`, as documented in the `photutils.isophote.Ellipse.fit_image` method.

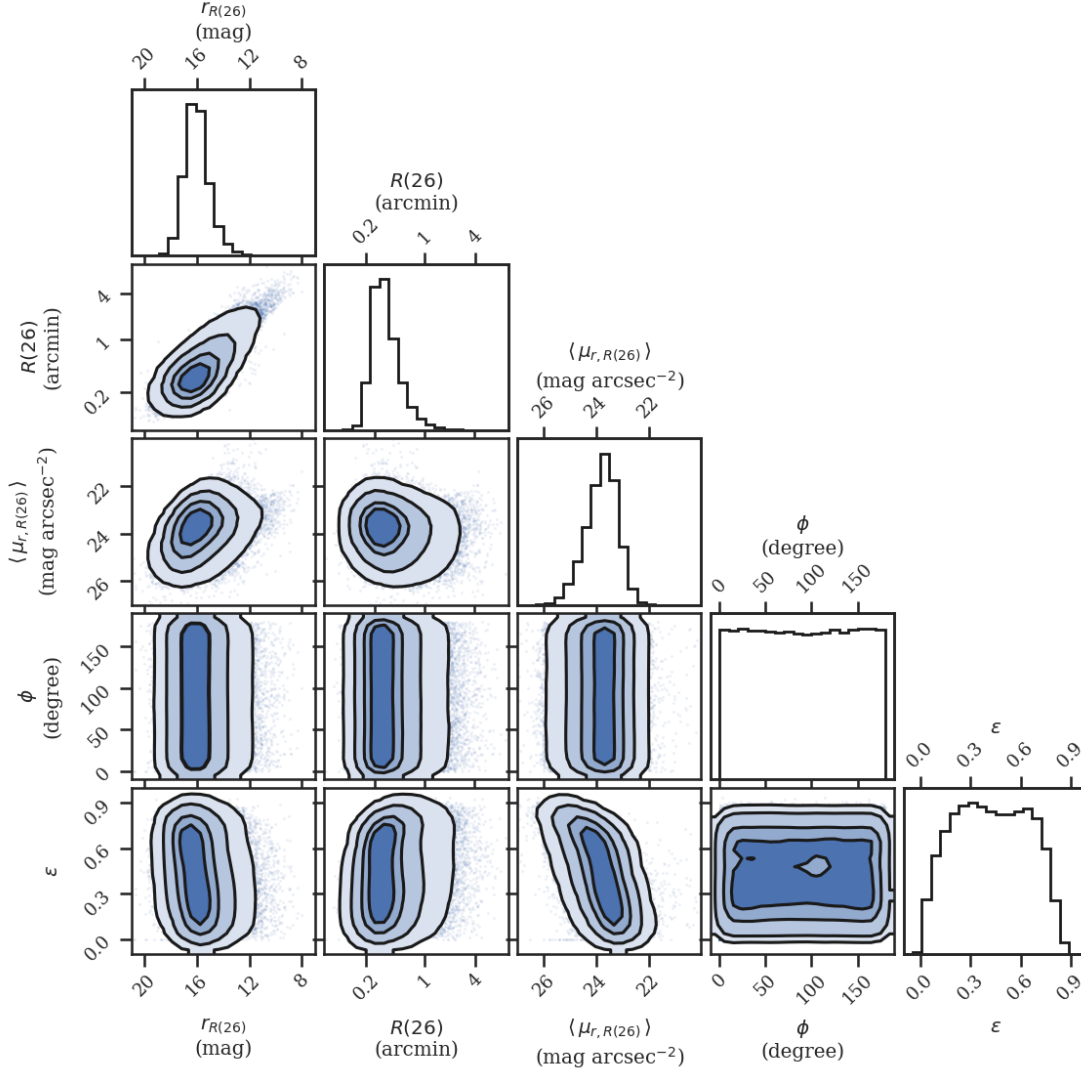


Figure 8. Multivariate distribution of a subset of measured SGA-2020 galaxy properties. From left to right along the bottom panels, we show $r_{R(26)}$, the r -band magnitude within $R(26)$, where $R(26)$ is the semi-major axis at the 26 mag arcsec $^{-2}$ isophote; $\langle \mu_{r,R(26)} \rangle$, the mean surface-brightness within $R(26)$; ϕ , the galaxy position angle; and ϵ , the galaxy ellipticity. The contours enclose 50%, 75%, 95%, and 99.5% of the blue points and have been smoothed by a 0.8-pixel Gaussian kernel.

26 mag arcsec $^{-2}$. We perform these measurements by fitting a linear model to the surface brightness profile converted to mag arcsec $^{-2}$ versus $r^{1/4}$ (which would be a straight line for a de Vaucouleurs galaxy profile), but only consider measurements which are within ± 1 mag arcsec $^{-2}$ of the desired surface brightness threshold. To estimate the uncertainty in the resulting radius, we generate 30 Monte Carlo realizations of the surface brightness profile and use the standard deviation of the resulting distribution of radii.

We also measure the curve-of-growth in each bandpass using the tools in `photutils.aperture`. Briefly, we integrate the image and variance image in each bandpass using elliptical apertures from the center of the galaxy to two times its estimated semi-major axis (based on the `ellipse moments`), again with a 1-pixel ($0''.262$) interval.²⁷ We fit the resulting curve-of-growth, $m(r)$, using the following empirical model:

$$m(r) = m_{\text{tot}} + m_0 \log_e \left[1 + \alpha_1 \left(\frac{r}{r_0} \right)^{-\alpha_2} \right], \quad (1)$$

where m_{tot} , m_0 , α_1 , α_2 , and r_0 are constant parameters of the model and r is the semi-major axis in arcseconds. In our analysis we take the radius scale factor $r_0 = 10''$ to be fixed (which makes α_1 dimensionless). Note that in the limit $r \rightarrow \infty$, m_{tot} is the total, integrated magnitude. Using this model, we infer the half-light semi-major axis length, r_{50} , analytically from the best-fitting model parameters,

$$r_{50} = r_0 \left\{ \frac{1}{\alpha_1} \left[\exp \left(-\frac{\log_{10}(0.5)}{0.4m_0} \right) - 1 \right] \right\}^{-1/\alpha_2}, \quad (2)$$

where r_{50} is measured in arcseconds and m_0 is in magnitudes.

3.3. Summary & Validation of SGA-2020 Data Products

The final SGA-2020 sample consists of 383,620 galaxies in the $\approx 20,000 \text{ deg}^2$ LS/DR9 imaging footprint. The final catalog contains precise coordinates; multi-wavelength mosaics; model images and photometry from `The Tractor`; azimuthally averaged optical surface-brightness profiles; aperture photometry and radii; and extensive metadata for all galaxies in this sample. In this section we briefly highlight some of these measurements; for a comprehensive description of the SGA-2020 data products and how they can be accessed, see Appendix B.

Figure 7 shows the celestial positions of the galaxies in the SGA-2020 in an equal-area Mollweide projection. The curved black line represents the Galactic plane, which divides the sample into the North Galactic Cap (NGC) and South Galactic Cap (SGC) imaging regions of the LS/DR9 footprint (see Dey et al. 2019). The total area subtended by the sample is $19,721 \text{ deg}^2$, covering nearly 50% of the sky.

In Figure 8 we highlight a handful of the measured SGA-2020 properties, as well as the relationships between them. In a multivariate corner plot (Foreman-Mackey 2016), we show $r_{R(26)}$, the r -band magnitude within $R(26)$, where $R(26)$ is the semi-major axis at the 26 mag arcsec⁻² isophote; $\langle \mu_{r,R(26)} \rangle \equiv r_{R(26)} + 2.5 \log_{10} [\pi R^2(26)]$, the average r -band surface-brightness within $R(26)$; ϕ , the galaxy position angle (measured counter-clockwise from North to East); and $\epsilon \equiv 1 - b/a$, the galaxy ellipticity, where b/a is the minor-to-major axis ratio. Note the expected strong correlation

²⁷ Unfortunately, our original elliptical aperture photometry had an irrecoverable bug, so in the final release of the SGA-2020 we infer the aperture photometry from the surface brightness profiles; see Appendix C for details.

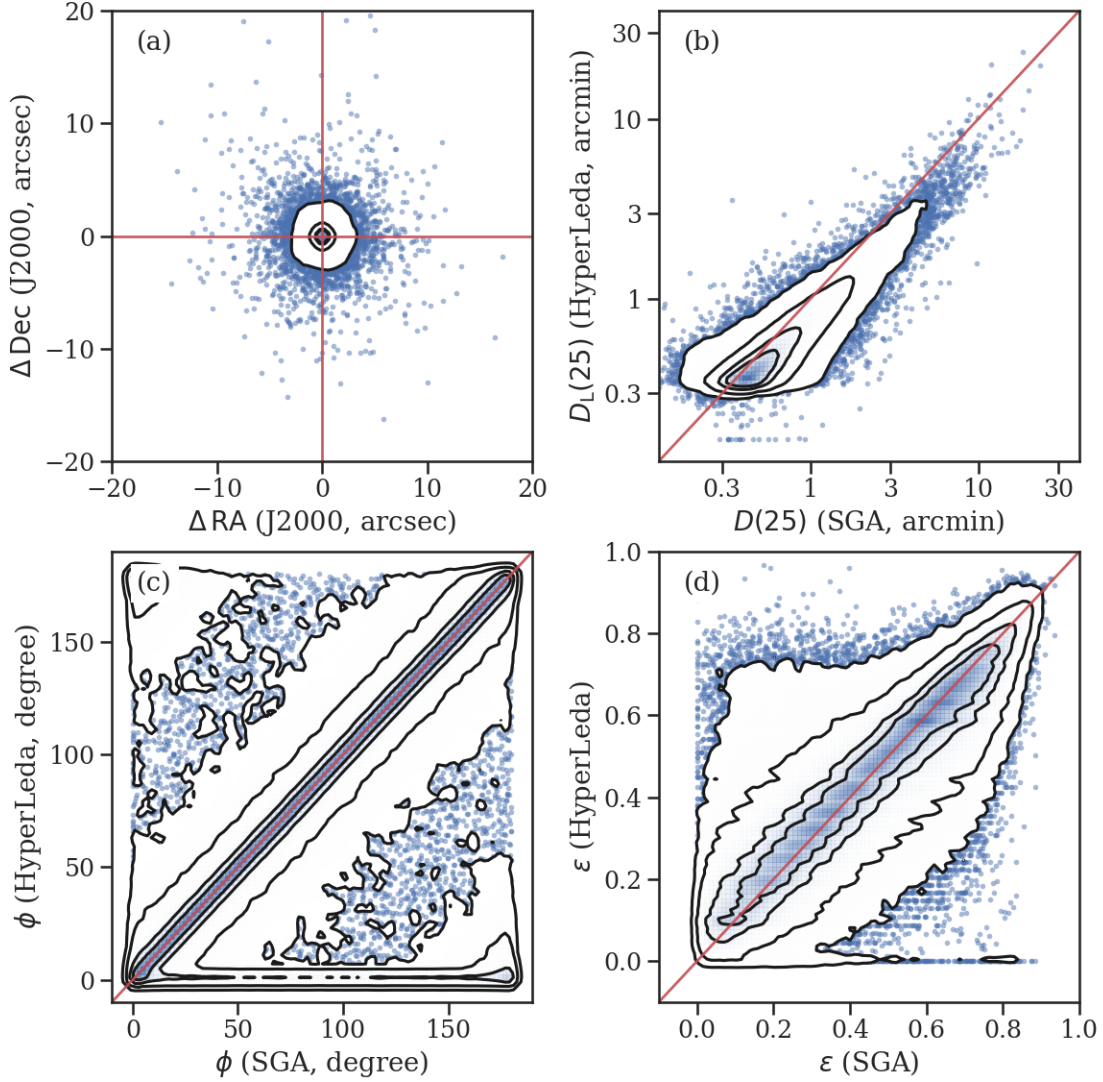


Figure 9. Comparison of select observed properties reported in HyperLeda against the newly measured quantities in the SGA-2020. (a) Difference in central coordinates; (b) $D_L(25)$ versus $D(25)$, the major-axis diameter measured at the 25 mag arcsec $^{-2}$ isophote; (c) galaxy position angle, ϕ ; and (d) galaxy ellipticity, $\epsilon \equiv 1 - b/a$, where b/a is the minor-to-major axis ratio. In every panel, the contours enclose 50%, 75%, 95%, and 99.5% of the blue points and have been smoothed by a 0.8-pixel Gaussian kernel. In panels (b), (c), and (d), the solid red line represents the one-to-one relation.

between $R(26)$ and $r_{R(26)}$, and the anti-correlation between ϵ and $\langle \mu \rangle_{r,R(26)}$, which is due to the light in more edge-on galaxies being attenuated more by the larger column of internal dust attenuation (famously known as the Holmberg “transparency test”; Holmberg 1958; Giovanelli et al. 1994).

In Figure 9 we compare some of the new geometrical measurements in the SGA-2020 against the measurements collated in HyperLeda. In panel (a) we plot ΔDec versus ΔRA , the difference in equatorial coordinates. The overall agreement in positions is

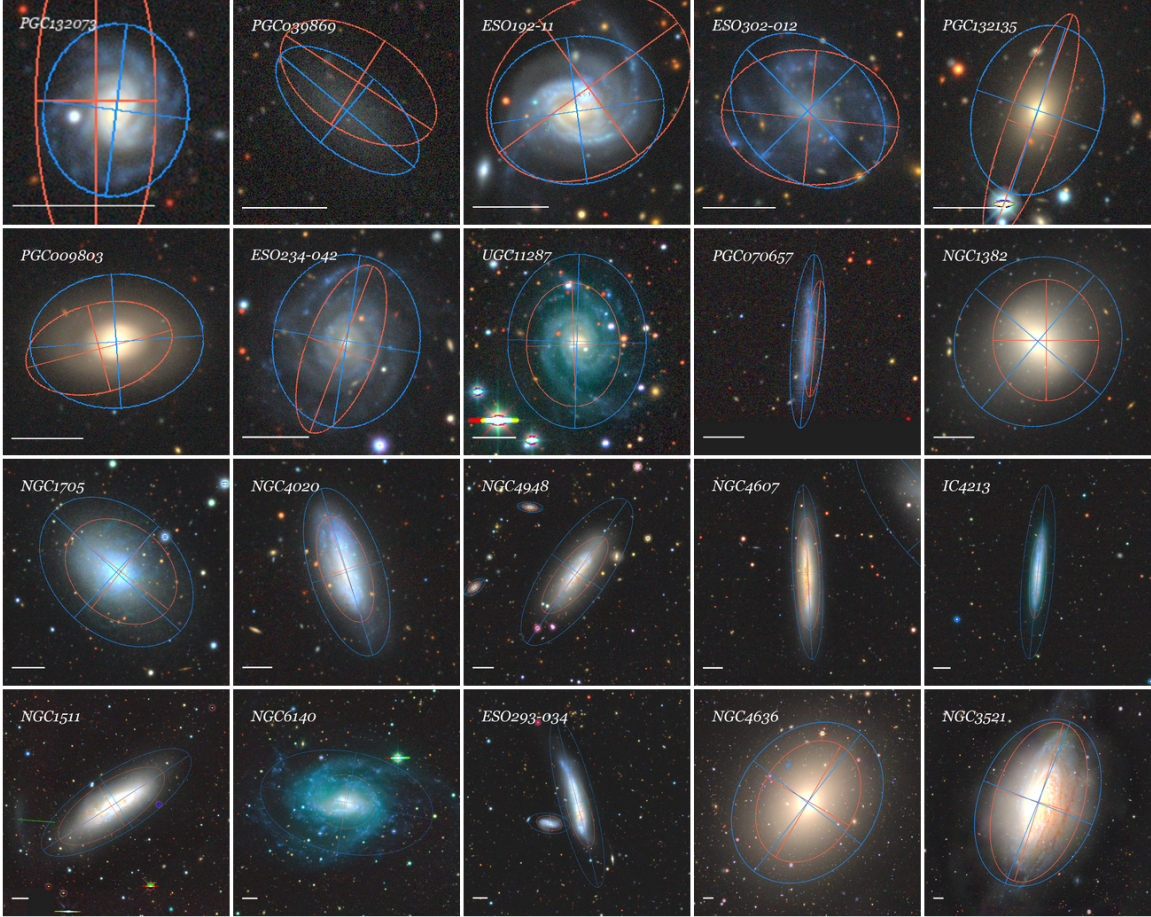


Figure 10. Randomly selected gallery of 20 galaxies where the light-weighted central coordinates measured in the SGA-2020 differ by more than $3''$ from the coordinates published in HyperLeda, sorted by increasing $D_L(25)$ from the upper-left to the lower-right. The white bar in the lower-left corner of each panel represents $30''$, and the blue and red cross-haired ellipses represent the SGA-2020 and HyperLeda positions and mean geometry, respectively. Although the centers of some of these systems are somewhat ambiguous due to dust lanes and other irregular features (e.g., NGC4607), the SGA-2020 coordinates are generally superior.

very good; the median, mean, and $\pm 1\sigma$ scatter are $0''.3$, $0''.4$, and $\pm 0''.5$, respectively, although the coordinates of individual (especially irregular and low surface-brightness) galaxies differ by up to tens of arcseconds. In Figure 10 we show a randomly selected set of 20 galaxies where the central coordinates in the SGA-2020 and HyperLeda differ by more than $3''$. Although reasonable algorithms may disagree about the central positions of some galaxies due to dust lanes or the lack of a prominent central bulge (e.g., NGC4948=IC4156 and ESO293-034), it is clear that the coordinates in the SGA-2020 for most of the examples highlighted in Figure 10 are more accurate in measuring the centroid of galaxies with bright cores and the center-of-light for more diffuse systems, even for very large, well-known galaxies like NGC4636=UGC07878 and NGC3521=UGC06150.

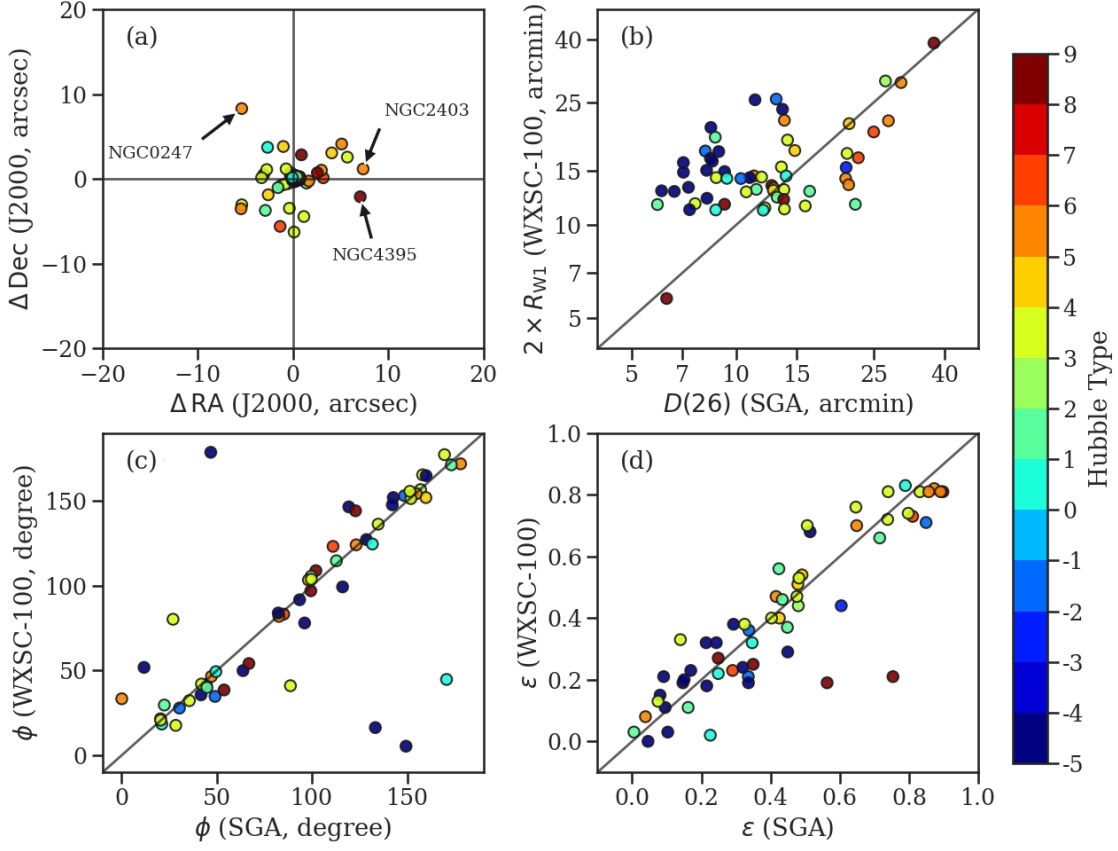


Figure 11. Comparison of the (a) central coordinates; (b) diameters; (c) position angles, ϕ ; and (d) ellipticities, ϵ measured in the SGA-2020 against those reported in the WXSC-100 (Jarrett et al. 2019) for an overlapping sample of 59 galaxies. Individual galaxies are color-coded by numerical Hubble type, from -5 (E) to 9 (Irr) (see de Vaucouleurs et al. 1991), as indicated by the colorbar. See the text in §3.3 for the definition of the diameter measured in the WXSC-100 catalog and a detailed discussion of the observed trends.

Next, in Figure 9(b) we plot $D_L(25)$ (defined in §2.1) versus $D(25)$, the SGA-2020 major-axis diameter measured at the 25 mag arcsec⁻² isophote. Not unexpectedly, we find a strong correlation between the two quantities, although $D(25)$ is $\approx 20\%$ larger, on average, than $D_L(25)$, presumably due to the deeper optical imaging used in the SGA-2020. Finally, in Figure 9(c) and 9(d) we plot the correlation between position angle, ϕ , and ellipticity, ϵ , respectively, between HyperLeda and the SGA-2020. For more than 95% of the sample, the agreement between the two ϕ and ϵ measurements are excellent.

In order to validate our measurements further, in Figure 11 we compare the SGA-2020 coordinates and mean geometrical measurements against the *WISE* Extended Source Catalog of the 100 Largest Galaxies (hereafter, WXSC-100; Jarrett et al. 2019).²⁸ Of the 104 galaxies in the WXSC-100 sample, 59 are in the LS/DR9 imag-

²⁸ <https://vislab.idia.ac.za/research-wxsc>

ing footprint and consequently in the SGA-2020. Note that WISE imaging is less affected by dust extinction and more sensitive to the underlying spatial distribution of the older stellar population compared to our optical imaging, so we do expect some differences in these measurements.

Focusing on panel (a) of Figure 11 first, we find good overall agreement in the central coordinates: the median, mean, and $\pm 1\sigma$ scatter in the coordinate differences are $0''.76$, $2''.3$, and $\pm 2''.4$, respectively, notably smaller than the $\approx 6''$ FWHM WISE W1 point-spread function (Wright et al. 2010). However, there are some notable outliers, the three largest of which (NGC0247, NGC2403, and NGC4395) have been annotated in the figure. Examining the optical and infrared mosaics of these and other sources in this comparison sample, we find that the differences are due to a combination of a lack of a distinct bright center and, for a handful of cases, errors in the SGA-2020. For example, both NGC2403 and NGC0247 are late-type spirals (Hubble type 6 or SABc; see de Vaucouleurs et al. 1991) without a clear, bright nucleus, so the differences are arguably defensible. On the other hand, for NGC4395 and a handful of other objects, the SGA-2020 central coordinates are likely incorrect (by up to $\approx 7''$) relative to those published in the WSXC-100 (see §6 for additional discussion).

Turning next to Figure 11(b), we compare $D(26)$ in the SGA-2020 to $2 \times R_{W1}$ in the WSXC-100; two times the radius of the galaxy measured down to an isophotal level of $\mu_{W1,AB} \approx 25.7$ mag arcsec $^{-2}$. We find the two sizes to be reasonably well-correlated, despite the differences in imaging effective wavelength, albeit divided into two broad sequences. The sizes of the spirals (Hubble types 2 to 3—Sab to Sb) and later generally follow the one-to-one relation (median difference of -0.004 dex) with a scatter of 0.11 dex ($\pm 30\%$), while the earlier-type, spheroidal galaxies (Hubble types -5 to 1—E to Sa) are offset to larger sizes in the WSXC-100 by -0.25 dex ($\approx 70\%$) with a scatter of 0.16 dex ($\pm 50\%$). As discussed by Jarrett et al. (2019), the WISE W1-band is very sensitive to light from evolved stars down to low surface-brightness levels (particularly due to its large pixels, $2''.75$), so it is not surprising for the WSXC-100 (infrared) diameters to be notably larger than the (optical, r -band) $D(26)$ diameters in the SGA-2020. Moreover, the extended, low surface-brightness envelopes of massive spheroidal galaxies are especially prone to over-subtraction (e.g., Blanton et al. 2011; Bernardi et al. 2013), which may also be contributing to the systematically smaller sizes of the early-type galaxies in the SGA-2020 relative to the WSXC-100 (see also §6).

Finally, in panels (c) and (d) of Figure 11, we compare the position angles and ellipticities reported in the SGA-2020 and WSXC-100 catalogs, respectively, and find very good agreement: the mean differences are $\phi_{\text{SGA}} - \phi_{\text{WSXC}} = 0^\circ 83 \pm 7.7$ and $\epsilon_{\text{SGA}} - \epsilon_{\text{WSXC}} = 0.017 \pm 0.12$.

4. CATALOG COMPLETENESS

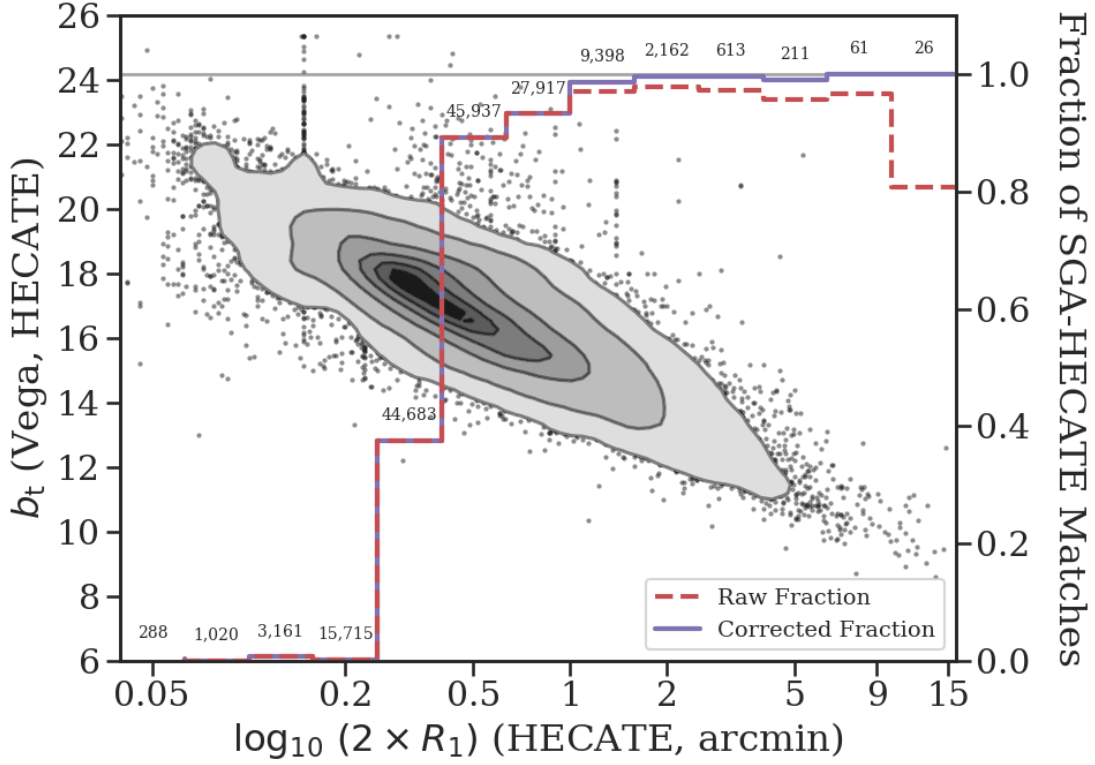


Figure 12. b_t -band magnitude versus $2 \times R_1$ for 154,093 objects in the HECATE value-added galaxy catalog (Kovlakas et al. 2021) which lie within the LS/DR9 imaging footprint, where R_1 is the semi-major axis length in HECATE. For reference, the contours enclose 10%, 25%, 50%, 75%, 95%, and 99% of the points. The dashed-red and solid purple histograms (corresponding to the right-hand vertical axis) represent, respectively, the raw and corrected fraction of HECATE galaxies which match a source in the SGA-2020 galaxy as a function of angular diameter. Finally, the small numbers written above each bin of the histograms report the number of HECATE galaxies in that 0.2-dex wide bin.

Quantifying the completeness of the SGA-2020 is difficult because the parent sample is largely defined by HyperLeda (see §2.1), which aggregates data from many different surveys—each with their own potentially complicated selection function—from the ultraviolet to the radio. This heterogeneity can be clearly seen in Figure 7 as variations in the sample surface density on both large and small angular scales and between the North and South Galactic Cap. Indeed, as we discuss in §6, one of the primary goals of the next version of the SGA is to redefine the parent sample using the Legacy Surveys imaging itself, in order to begin with a more uniform and quantifiable selection function over the full area. Nevertheless, we can still assess the SGA’s completeness by comparing against existing catalogs which include large angular-diameter galaxies.

We choose to characterize the completeness of the SGA-2020 by comparing against HECATE (version 1.1; Kowlakas et al. 2021).²⁹ HECATE is an all-sky value-added catalog of $\approx 200,000$ galaxies at $z < 0.047$ ($\lesssim 200$ Mpc) which contains a breadth of both observed and derived (physical) galaxy properties. Although HECATE also uses HyperLeda to define its parent sample, the comparison is still valuable because the analysis carried out by Kowlakas et al. (2021) is independent of ours, and it includes additional completeness checks against NED and against the local B -band luminosity function.

First, from the parent HECATE sample of 204,733 galaxies, we identify 154,093 objects (75%) to be within the LS/DR9 imaging footprint using the LS/DR9 random catalogs, which contain a wealth of information about the imaging data (bandpass coverage, depth, PSF size, etc.) at random positions over the footprint (Myers et al. 2023).³⁰ Specifically, we merge together five random catalogs to achieve an effective source density of $12,500 \text{ deg}^{-2}$, and conservatively retain all HECATE objects whose center lies within $2'$ of one of these points. Next, we remove 2844 galaxies without any size information in HECATE; visually inspecting a random subset of these reveals that they are predominantly small objects, $D(25) \ll 30''$, well under the SGA-2020 angular diameter limit (Figure 4). Finally, from the remaining 151,249 objects, we match 95,800 (63%) of them to an object in the SGA-2020 using the HyperLeda PGC number (Paturel et al. 1989; Makarov et al. 2014), which both HECATE and the SGA-2020 record (where it is defined). We choose to use the PGC designation because the differences in coordinates can be significant, such that a single matching radius results in a non-negligible number of false-positives. For example, among the PGC-matched samples, the mean difference in coordinates is $0':50 \pm 0':92$, but with a tail which extends out to $80''$ for IC2574, a well-known $18'.7$ -diameter late-type (SABm) galaxy with no well-defined center. In fact, 126 PGC-matched galaxies have coordinate differences larger than $10''$, 90% of which have $D(26) > 1'$. Nevertheless, with these caveats in mind, we can still match an additional 178 objects using a $3''$ matching radius, resulting in a final matched sample of 95,978 galaxies.

In Figure 12 we plot b_t -band magnitude versus $2 \times R_1$ for the 154,093 HECATE galaxies which overlap the LS/DR9 footprint, where R_1 is the semi-major axis length reported in HECATE. The dashed red histogram (corresponding to the right-hand axis), shows the *raw* fraction of matching HECATE-SGA galaxies as a function of galaxy size, in uniform 0.2-dex wide bins of angular diameter between $\approx 2''$ and $\approx 15'.8$. The small numbers written above each bin of the histogram report the number of HECATE galaxies in that bin. In addition, the horizontal gray line indicates, for reference, a matching fraction of 100%.

Taken at face value, the (raw) matching fractions shown in Figure 12 are surprisingly poor. For example, these results suggest that the SGA-2020 is missing 3% – 5% of

²⁹ <https://hecate.ia.forth.gr>

³⁰ <https://www.legacysurvey.org/dr9/files/#random-catalogs-randoms>

galaxies with angular diameters between $2'.5$ and $10'$ and a whopping 20% of the galaxies between $10'$ and $16'$. In total, we find 2.94% (367/12,487) of the HECATE galaxies with $2 \times R_1 > 1'$ to be missing from the SGA-2020. To explore this purported incompleteness, we visually inspect the LS/DR9 imaging at the position of the 367 “missing” galaxies and find the following results: 20 objects are Local Group dwarf galaxies which are intentionally excluded from the SGA-2020 (see §2.1); 44 objects fall on the edge of the imaging footprint or other serendipitous (but unfortunate) gaps in three-band (*grz*) coverage; 64 galaxies are real but the angular diameters reported in HECATE are overestimated, sometimes by a significant factor; 78 are part of a larger galaxy (e.g., H II regions) and other kinds of photometric shreds; and 24 are entirely spurious. The solid purple histogram in Figure 12 shows the corrected fraction of HECATE-SGA matches after accounting for these errors. In the end, we find that just 137 out of 12,257 (1.12%) HECATE galaxies with $2 \times R_1 > 1'$ are real and genuinely missing from the SGA-2020.

Although the fraction of missing galaxies is relatively low, since both the SGA-2020 and HECATE ultimately originate (in large part) from HyperLeda, it is surprising that *any* objects are missing from the SGA-2020, especially ones with angular diameters larger than one arcminute. Although we do not know why these objects do not appear in our parent HyperLeda catalog, we suspect that an issue with the database query may be ultimately responsible (see Appendix A). In any case, we intend to ensure that these and other missing objects serendipitously identified by the SGA team through visual inspection are included in the next version, as we discuss in §6.

What about the completeness of the SGA-2020 among smaller angular-diameter galaxies, $25'' \lesssim 2 \times R_1 < 1'$? According to Figure 12, the completeness remains relatively high, above $\approx 90\%$. However, our analysis of the $> 1'$ -diameter galaxies reveals that more than half of the HECATE objects missing from the SGA-2020 either have incorrect (or overestimated) diameters, or are spurious, and we have checked that these and other effects increase steeply with decreasing angular diameter (see, for example, Figure 2). Therefore, we conclude that the SGA-2020 completeness is likely $\gtrsim 95\%$ for galaxies with angular diameters between $\approx 25''$ and $1'$.

None of this discussion, of course, addresses the surface-brightness incompleteness of the sample, since both HECATE and the SGA-2020 inherit whatever incompletenesses and heterogeneities are present in HyperLeda, which aggregates data from many different surveys. For example, regions of the sky which have been imaged by the SDSS (Strauss et al. 2002; Blanton et al. 2011) or DES (Dark Energy Survey Collaboration et al. 2016; Abbott et al. 2021) have uniform, deep optical imaging ($\mu_{r,50} < 24.5$ and $\mu_r < 25.6$ mag arcsec $^{-2}$ in the SDSS and DES, respectively, where $\mu_{r,50}$ is the *r*-band half-light surface brightness and the DES surface brightness is measured in a $1''.95$ diameter aperture), but these surveys cover just 34% (SDSS; 14,000 deg 2) and 12% (DES; 5,000 deg 2) of the sky. Other optical and near-infrared surveys like 2MASS (Jarrett et al. 2000; Skrutskie et al. 2006) and Pan-STARRS1

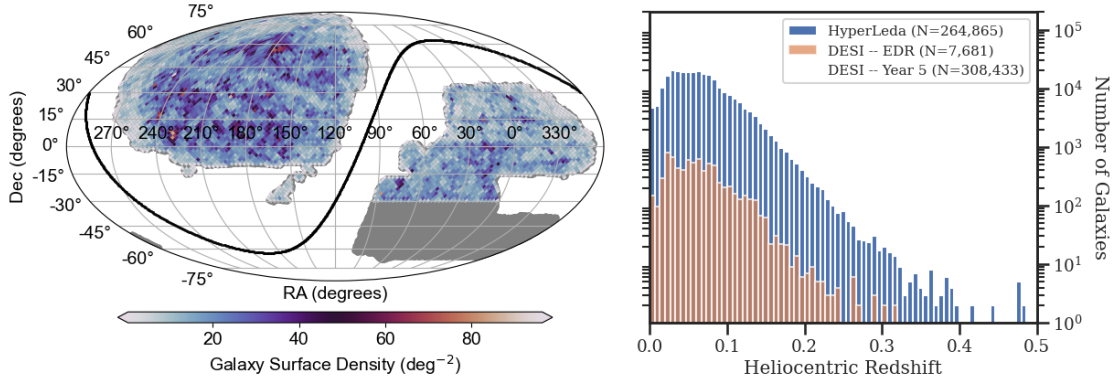


Figure 13. (Left) Celestial distribution of galaxies in the SGA-2020 which are also DESI targets (*colorbar*) covering $\approx 14,000 \text{ deg}^2$ (Myers et al. 2023) compared to the full $\approx 20,000 \text{ deg}^2$ footprint of the SGA-2020 (*dark gray region* in the SGC). (Right) Redshift distribution of galaxies in the SGA-2020 with existing spectroscopic redshifts from HyperLeda (*blue histogram*) and from the DESI Early Data Release (EDR; *orange histogram*). The legend in this figure also indicates the approximate final number of SGA-2020 galaxies which DESI will observe by the end of the five-year Main Survey.

(PS1; Chambers et al. 2016) cover all or nearly all of the sky (100% and 75% for 2MASS and PS1, respectively); however, 2MASS is relatively shallow compared to these other surveys ($\mu_r \approx 22.7 \text{ mag arcsec}^{-2}$ assuming a median $r - K_s \approx 2.7$ color for low-redshift galaxies; Jarrett et al. 2019) while the photometry of bright, large angular-diameter galaxies in PS1 is known to be problematic (Magnier et al. 2020; Makarov et al. 2022). In other words, it is difficult to fully assess the incompleteness of the SGA-2020 given the variations in the completeness of the surveys which contribute to HyperLeda.

Nevertheless, we can still make some quantitative statements using the results shown in Figure 8 and the comparisons with HECATE, above. Based on the correlation between the mean surface-brightness, $\langle \mu_{r,R(26)} \rangle$, and the apparent brightness within the 26 mag arcsec $^{-2}$ isophote, $r_{R(26)}$, we conclude that the SGA-2020 is approximately 95% complete for galaxies with $R(26) \gtrsim 25''$, $r_{R(26)} \lesssim 18$, and $\langle \mu_{r,R(26)} \rangle \lesssim 26 \text{ mag arcsec}^{-2}$; in addition, the SGA-2020 is more than 99% complete for galaxies larger than $1'$ and brighter than $r_{R(26)} \lesssim 16$ down to the same surface-brightness limit.

5. SCIENTIFIC APPLICATIONS

As discussed in the introduction, atlases of large angular-diameter galaxies have played a pivotal role in observational cosmology and in our modern understanding of galaxy astrophysics and the galaxy-halo connection. By delivering a carefully constructed catalog of known “large” galaxies with new deep optical and infrared imaging from the DESI Legacy Imaging Surveys, we anticipate the SGA-2020 to play

a commensurately high-impact role in a wide range of observational studies of large, nearby, well-resolved galaxies.

The growing spectroscopic dataset from DESI is an especially powerful complement to the SGA-2020. As discussed in §1.2, DESI is targeting the SGA-2020 sample over $14,000 \text{ deg}^2$ (70% of the LS/DR9 footprint) as part of the flux-limited ($r < 20.175$) Bright Galaxy Survey (BGS; Hahn et al. 2023).³¹ In addition to providing precise spectroscopic redshifts, the spectral coverage (3600–9800 Å), instrumental resolution ($\mathcal{R} \approx 2000 - 5000$), and spectrophotometric precision ($\pm 2\%$) of the DESI spectra (Abareshi et al. 2022; Guy et al. 2023) will yield important insights into the physical conditions and stellar populations of the central regions of these systems (for recent reviews, see Conroy 2013, Kewley et al. 2019, Sánchez 2020, and references therein).

Figure 13 illustrates the tremendous scale of the DESI dataset. Although the majority of galaxies in the SGA-2020 have previously measured redshifts in HyperLeda (264,865 galaxies, or approximately 70% of the sample), these redshifts come from a wide range of different surveys spanning many decades. By the end of its five-year Main Survey (2021-2026), DESI will produce a homogeneous, high-precision spectrophotometric dataset for more than 300,000 SGA-2020 targets over $14,000 \text{ deg}^2$ as part of a larger sample of approximately 14 million BGS targets and more than 25 million fainter extragalactic targets (Myers et al. 2023; DESI Collaboration et al. 2023b). Indeed, in its June 2023 Early Data Release (EDR), DESI has already delivered high-quality spectroscopy for nearly 7700 SGA-2020 targets which were observed during the DESI Survey Validation period (DESI Collaboration et al. 2023a).³²

In addition to these Main-Survey observations, one of the especially exciting and synergistic *secondary* DESI programs is the Peculiar Velocity survey (Saulder et al. 2023).³³ This program aims to use the Fundamental Plane and Tully–Fisher relations as direct distance indicators in order to map the peculiar velocity field at $z < 0.15$; this map will be used to place new, stringent constraints on the cosmological parameters and the growth of large-scale structure (e.g., Strauss & Willick 1995). As part of this effort, galaxies in the SGA-2020 are being targeted not only in their bright nucleus but also at various positions along their major axis and other “off-center” positions (Saulder et al. 2023; Douglass et al. 2023, in prep.). Together with the central spectra, these data will help constrain the total (dynamical) masses and physical conditions in a sample of tens of thousands of SGA-2020 galaxies.

The SGA-2020 also has the potential to support the growing number of time-domain and multi-messenger astronomical discoveries, wherein observations of transient astrophysical events are detected by one or more *messenger particles* (electromagnetic radiation, neutrinos, cosmic rays, and gravitational waves; e.g., Neronov 2021). In the

³¹ In detail, BGS is observing all galaxies brighter than $r = 19.5$ (BGS Bright) and a color-selected subset of galaxies with $19.5 < r < 20.175$ (BGS Faint); the color selection is tuned to ensure good redshift success at this flux level in bright sky conditions.

³² <https://data.desi.lbl.gov/doc/releases/edr>

³³ Secondary programs are bespoke scientific programs which utilize whatever spare fibers may be available in a given DESI tile or pointing of ~ 5000 fibers (see Myers et al. 2023 for details).

case of gravitational wave events, for example, identifying the host galaxy and, ideally, the electromagnetic counterparts of these events is extremely challenging due to the significant positional error ellipse of gravitational wave observations, $\gtrsim 100 \text{ deg}^2$ (Gehrels et al. 2016; Abbott et al. 2020). Statistically complete catalogs of large, nearby galaxies with accurate coordinates, size information, and multi-band photometry like the SGA-2020 are needed to help identify the most likely source of gravitational wave events (e.g., Gehrels et al. 2016; Ducoin et al. 2020; Kowlakas et al. 2021).

Finally, we highlight one other area where the SGA-2020 is playing an important ancillary role. The SGA-2020 is being used as a foreground *angular mask* for all the DESI dark-time cosmological tracers: luminous red galaxies (LRGs; Zhou et al. 2023); emission-line galaxies (ELGs; Raichoor et al. 2023); and quasars (QSOs; Chaussidon et al. 2023). Like bright stars, large angular-diameter galaxies can bias the small-scale clustering signal in cosmological analyses because photometric pipelines tend to *shred* structurally resolved galaxies into many smaller sources. Similarly, the same angular mask can be used as an external input when building photometric catalogs from other imaging data; for example, an early version of the SGA-2020 was used to maximize the purity of the $3 - 5 \mu\text{m}$ unWISE photometric catalog of two billion infrared sources (Schlafly et al. 2019). In other words, by providing a high-quality geometric mask, the SGA-2020 is helping these and other observational programs fulfill their scientific promise.

6. SUMMARY & FUTURE WORK

We present the 2020 version of the Siena Galaxy Atlas, SGA-2020, a multi-wavelength optical and infrared imaging atlas of 383,620 large angular-diameter galaxies covering $\approx 20,000 \text{ deg}^2$.³⁴ The SGA-2020 contains precise coordinates; optical (*grz*) and WISE/W1 through W4 ($3.4 - 22 \mu\text{m}$) infrared mosaics; model images and photometry based on the state-of-the-art image modeling code, **The Tractor**; azimuthally averaged *grz* surface-brightness and color profiles; elliptical curves of growth and half-light radii; and extensive ancillary information for the full sample. The complete SGA-2020 can be accessed through the dedicated web-portal, <https://sga.legacysurvey.org>.

Our measurements of the central coordinates, isophotal diameters, ellipticities, and position angles show overall good agreement with published measurements collated in the HyperLeda extragalactic database and in the WISE Extended Source Catalog of the 100 Largest Galaxies (WXSC-100; Jarrett et al. 2019). Disagreements in these quantities between the SGA-2020 and HyperLeda are generally due to erroneous measurements in HyperLeda; however, the comparison with WXSC-100 identifies

³⁴ Excluding the highest regions of dust extinction in the Galactic plane, $|b| > 20^\circ$, the SGA-2020 covers 74% of the available $\approx 27,200 \text{ deg}^2$ of extragalactic sky.

small but notable (\approx few arcsecond) errors in the SGA-2020 coordinates for some of the largest ($> 5'$) galaxies in the sample.

We evaluate the completeness of the SGA-2020 by comparing against the HECATE all-sky, value-added galaxy catalog (Kovlakas et al. 2021). We find that the SGA-2020 is missing approximately 1% of known galaxies larger than one arcminute and $\approx 5\%$ of galaxies between $25''$ and $1'$; however, we compute these statistics only after determining (through visual inspection) that nearly 30% of the sources larger than $1'$ in HECATE which are missing from the SGA-2020 are either spurious or photometric shreds. Overall, we estimate that the SGA-2020 is more than 95% complete for galaxies larger than $R(26) \approx 25''$ and $r < 18$ measured at the 26 mag arcsec $^{-2}$ isophote in the r -band.

We discuss some of the potential scientific applications of the SGA-2020 and highlight the ongoing amassing of high-quality optical spectrophotometry from the Dark Energy Spectroscopic Instrument (DESI; DESI Collaboration et al. 2023b) survey. Approximately 70% of the SGA-2020 sample lies within the 14,000 deg 2 DESI footprint and is being targeted as part of the Bright Galaxy Survey (BGS; Hahn et al. 2023). To date, 7700 DESI spectra of SGA-2020 galaxies are publicly available as part of the DESI Early Data Release (EDR; DESI Collaboration et al. 2023a), representing less than 3% of the final sample. In addition, the DESI Peculiar Velocity secondary program (Saulder et al. 2023) is obtaining tens of thousands of major-axis, minor-axis, and other off-center spectra of SGA-2020 galaxies in order to constrain the peculiar-velocity field at $z < 0.15$, further enhancing the scientific impact of the SGA-2020. Finally, we highlight the potential impact of the SGA-2020 for identifying the electromagnetic counterparts of time-domain and multi-messenger astronomical events.

We conclude by discussing some of the planned improvements of the Siena Galaxy Atlas. Future versions will focus on four broad areas, listed here in no particular order:

- Completeness—As discussed in §4, the SGA-2020 inherits the heterogeneity and incompleteness of the parent HyperLeda sample. To mitigate these issues, we intend to build a new parent sample of candidate large angular-diameter galaxies by detecting them from the Legacy Surveys imaging data themselves using a combination of traditional source-detection techniques (e.g., convolution kernels optimized for detecting large galaxies) and one or more state-of-the-art deep-learning techniques (e.g., Stein et al. 2022; Zaritsky et al. 2023). By inserting artificially generated galaxies of varying size, integrated flux, and surface-brightness into the data, we intend to quantify the completeness limits of the sample as a function of these observational quantities.
- Centroiding and masking—Another area of improvement is how the SGA pipeline handles mergers and other systems with two or more close compan-

ions (e.g., in dense cluster environments like the Coma Cluster), as well as galaxies near bright stars. Evaluating and optimizing the performance of the pipeline in these circumstances will be part of a larger visual inspection effort (e.g., [Walmsley et al. 2022](#)) to ensure that the central coordinates of the largest galaxies in the SGA-2020 are accurate (or at least defensible, in the case of galaxies with irregular morphologies) compared with previous independent measurements (e.g., see the discussion in §3.3).

- Background-subtraction—As discussed in §3.2.1, aggressive subtraction of the Mosaic-3 pattern-noise significantly impacts the z -band photometry of the SGA-2020 galaxies in the northern (BASS+MzLS) portion of the footprint, $\text{Dec} \gtrsim 32^\circ$, including some of the most famous and largest angular-diameter galaxies in the sample like NGC5194=M51a and NGC5457=M101. Moreover, we show in §3.3 that the outer envelopes of the early-type, spheroidal galaxies in the atlas have likely been over-subtracted, thereby biasing their surface-brightness profiles and inferred isophotal diameters. We intend to address both these issues in a future version of the SGA (see, for example, [Li et al. 2022](#) for a new sky-subtraction technique which addresses the latter issue).
- Extensions in footprint and wavelength—Since the SGA-2020 was finalized, thousands of square degrees of additional DECam imaging have been acquired; we intend to use these data to extend the SGA footprint.³⁵ In addition, in the next version of the SGA we intend to (1) include DECam i -band imaging, which is available for more than 15,000 deg^2 of area; (2) regenerate the unWISE coadds but also add ultraviolet (1528 Å and 2271 Å) coadds from the Galaxy Evolution Explorer (GALEX; [Martin et al. 2005](#); [Morrissey et al. 2005](#)), where GALEX data are available; and (3) measure the surface-brightness profiles in all the available bandpasses from 0.15 to 22 μm . These additional measurements will further increase the scientific impact and long-term legacy value of the SGA.

Finally, future version of the SGA will also include ancillary spectroscopic redshifts and spectrophotometric measurements from DESI and, eventually, a wide range of physical properties (stellar masses, star-formation rates, etc.) derived using state-of-the-art spectral energy distribution modeling ([Moustakas et al. 2023](#), in prep.; [Leja et al. 2017](#)).³⁶

ACKNOWLEDGMENTS

We gratefully acknowledge specific contributions and thoughtful feedback from Michael Blanton, Yao-Yuan Mao, and Kevin Napier, and from former Siena College undergraduate students Alissa Ronca and Luis Villa, who contributed to an early

³⁵ See, e.g., <https://www.legacysurvey.org/dr10>.

³⁶ <https://fastspecfit.readthedocs.io/en/latest>

version of the SGA web-application. In addition, we thank Mara Salvato for helpful comments on a draft of the paper.

JM gratefully acknowledges funding support from the U.S. Department of Energy, Office of Science, Office of High Energy Physics under Award Number DE-SC0020086 and from the National Science Foundation under grant AST-1616414. ADM was supported by the U.S. Department of Energy, Office of Science, Office of High Energy Physics, under Award Number DE-SC0019022. AD, SJ, and BAW's research activities are supported by the NSF's NOIRLab, which is managed by the Association of Universities for Research in Astronomy (AURA) under a cooperative agreement with the National Science Foundation.

We acknowledge the use of the HyperLeda database and we are especially grateful for the time and expertise contributed by Dmitry Makarov to this project. This research has also made extensive use of the NASA/IPAC Extragalactic Database (NED), which is funded by the National Aeronautics and Space Administration and operated by the California Institute of Technology; NASA's Astrophysics Data System; and the arXiv preprint server.

The Legacy Surveys consist of three individual and complementary projects: the Dark Energy Camera Legacy Survey (DECaLS; Proposal ID #2014B-0404; PIs: David Schlegel and Arjun Dey), the Beijing-Arizona Sky Survey (BASS; NOAO Prop. ID #2015A-0801; PIs: Zhou Xu and Xiaohui Fan), and the Mayall z-band Legacy Survey (MzLS; Prop. ID #2016A-0453; PI: Arjun Dey). DECaLS, BASS and MzLS together include data obtained, respectively, at the Blanco telescope, Cerro Tololo Inter-American Observatory, NSF's NOIRLab; the Bok telescope, Steward Observatory, University of Arizona; and the Mayall telescope, Kitt Peak National Observatory, NOIRLab. The Legacy Surveys project is honored to be permitted to conduct astronomical research on Iolkam Du'ag (Kitt Peak), a mountain with particular significance to the Tohono O'odham Nation.

NOIRLab is operated by the Association of Universities for Research in Astronomy (AURA) under a cooperative agreement with the National Science Foundation.

This project used data obtained with the Dark Energy Camera (DECam), which was constructed by the Dark Energy Survey (DES) collaboration. Funding for the DES Projects has been provided by the U.S. Department of Energy, the U.S. National Science Foundation, the Ministry of Science and Education of Spain, the Science and Technology Facilities Council of the United Kingdom, the Higher Education Funding Council for England, the National Center for Supercomputing Applications at the University of Illinois at Urbana-Champaign, the Kavli Institute of Cosmological Physics at the University of Chicago, Center for Cosmology and Astro-Particle Physics at the Ohio State University, the Mitchell Institute for Fundamental Physics and Astronomy at Texas A&M University, Financiadora de Estudos e Projetos, Fundacao Carlos Chagas Filho de Amparo, Financiadora de Estudos e Projetos, Fundacao Carlos Chagas Filho de Amparo a Pesquisa do Estado do Rio de Janeiro,

Conselho Nacional de Desenvolvimento Científico e Tecnológico and the Ministerio da Ciencia, Tecnologia e Inovacao, the Deutsche Forschungsgemeinschaft and the Collaborating Institutions in the Dark Energy Survey. The Collaborating Institutions are Argonne National Laboratory, the University of California at Santa Cruz, the University of Cambridge, Centro de Investigaciones Energeticas, Medioambientales y Tecnologicas-Madrid, the University of Chicago, University College London, the DES-Brazil Consortium, the University of Edinburgh, the Eidgenössische Technische Hochschule (ETH) Zurich, Fermi National Accelerator Laboratory, the University of Illinois at Urbana-Champaign, the Institut de Ciències de l’Espai (IEEC/CSIC), the Institut de Física d’Altes Energies, Lawrence Berkeley National Laboratory, the Ludwig Maximilians Universität München and the associated Excellence Cluster Universe, the University of Michigan, NSF’s NOIRLab, the University of Nottingham, the Ohio State University, the University of Pennsylvania, the University of Portsmouth, SLAC National Accelerator Laboratory, Stanford University, the University of Sussex, and Texas A&M University.

BASS is a key project of the Telescope Access Program (TAP), which has been funded by the National Astronomical Observatories of China, the Chinese Academy of Sciences (the Strategic Priority Research Program “The Emergence of Cosmological Structures” Grant # XDB09000000), and the Special Fund for Astronomy from the Ministry of Finance. The BASS is also supported by the External Cooperation Program of Chinese Academy of Sciences (Grant # 114A11KYSB20160057), and Chinese National Natural Science Foundation (Grant # 11433005).

The Legacy Survey team makes use of data products from the Near-Earth Object Wide-field Infrared Survey Explorer (NEOWISE), which is a project of the Jet Propulsion Laboratory/California Institute of Technology. NEOWISE is funded by the National Aeronautics and Space Administration.

The Legacy Surveys imaging of the DESI footprint is supported by the Director, Office of Science, Office of High Energy Physics of the U.S. Department of Energy under Contract No. DE-AC02-05CH1123, by the National Energy Research Scientific Computing Center, a DOE Office of Science User Facility under the same contract; and by the U.S. National Science Foundation, Division of Astronomical Sciences under Contract No. AST-0950945 to NOAO.

Software: `Astropy` (Astropy Collaboration et al. 2013, 2018, 2022), `corner.py` (Foreman-Mackey 2016), `healpy` (Zonca et al. 2019), `NumPy` (Harris et al. 2020), `Matplotlib` (Hunter 2007), `Photutils` (Bradley 2023), `PyDL` (Weaver et al. 2019), `scipy` (Virtanen et al. 2020), `seaborn` (Waskom 2021).

A. HyperLeda DATABASE QUERY

In §2.1 we present our procedure for building the SGA-2020 parent sample, which begins with a HyperLeda database query. For the purposes of reproducibility, this Appendix documents the exact query we execute on the 2018 November 14 version of the HyperLeda database, which results in a catalog of 1,436,176 galaxies:

```
WITH
  "R50" AS
  (
    SELECT pgc, avg(lax) AS lax, avg(sax) AS sax
    FROM rawdia
    WHERE quality=0 and dcode=5 and band between 4400 and 4499 GROUP BY pgc
  ),
  "IR" AS
  (
    SELECT pgc, avg(lax) AS lax, avg(sax) AS sax
    FROM rawdia
    WHERE quality=0 and iref in (27129) and dcode=7 and band=0 GROUP BY pgc
  )
SELECT
  m.pgc, m.objname, m.objtype, m.al2000, m.de2000, m.type,
  m.bar, m.ring, m.multiple, m.compactness, m.t, m.logd25,
  m.logr25, m.pa, m.bt, m.it, m.kt, m.v, m.modbest,
  "R50".lax, "R50".sax, "IR".lax, "IR".sax,
FROM
  m000 AS m
  LEFT JOIN "R50" USING (pgc)
  LEFT JOIN "IR" USING (pgc)
WHERE
  objtype='G' and (m.logd25>0.2 or "R50".lax>0.2 or "IR".lax>0.2)
```

B. DATA PRODUCTS & DATA ACCESS

In this Appendix, we define the data model for the SGA-2020 data products and describe how all the data can be accessed. All the input imaging data used to construct the SGA-2020, including the six-year unWISE image stacks, are publicly accessible through <https://www.legacysurvey.org>. The SGA-2020 data themselves can be retrieved through the *SGA-2020 Data Portal* at <https://sga.legacysurvey.org>. This portal provides a searchable database for retrieving data and visualizations for individual galaxies, as well as bulk-download access to the full dataset. For example, the following link will navigate directory to the beautiful face-on spiral (Hubble type SABc) NGC2532: <https://sga.legacysurvey.org/group/NGC2532>. In addition, the data can be accessed (and cross-referenced against a growing number of

additional datasets, including DESI) through NSF’s NOIRLab Astro Data Lab at <https://datalab.noirlab.edu/sga.php>. Finally, one can interactively explore the sample in the Legacy Surveys imaging footprint via the *SGA layer* of the *Legacy Surveys Viewer*; for example, the following link will navigate to the position of NGC2532 in the North Galactic Cap: <https://www.legacysurvey.org/viewer?ra=122.5638&dec=33.9568&layer=ls-dr9&zoom=13&sga>.

Most users will be interested in the `SGA-2020.fits` file, a multi-extension FITS catalog which contains detailed information for all 383,620 galaxies in the SGA-2020. Table 1 summarizes the contents of this file and Table 2 contains a detailed description of the ELLIPSE Header/Data Unit (HDU). In addition, Table 3 defines the ELLIPSEBIT bit-masks which record issues associated with the ellipse-fitting and surface-brightness profile modeling, if any.

Furthermore, for each galaxy group in the atlas (i.e., each row in the `SGA-2020.fits` catalog where `GROUP_PRIMARY` is `True`), we generate the set of files summarized in Table 4 (see also §3.2), which include the individual multi-wavelength mosaics, Tractor catalogs, surface-brightness profiles, and other key data products. These files are organized into the directory structure `RASLICE/GROUP_NAME`, where `GROUP_NAME` is the name of the galaxy group (see §2.2) and `RASLICE`, which ranges between 000 and 359, is the one-degree wide slice of the sky that the object belongs to. Specifically, in Python:

```
RASLICE = "{:03d}".format(GROUP_RA)
```

Finally, Table 5 documents the data model of the ellipse-fitting and surface-brightness profile results for each individual galaxy in the SGA-2020.

C. KNOWN ISSUES

Not surprisingly, a catalog the size and complexity of the SGA-2020 has imperfections, most of which were identified after the fitting was finalized. In this Appendix we document the currently known issues, all of which we intend to address in future versions of the SGA. For additional details and the most up-to-date documentation regarding these and other issues, we refer the interested reader to <https://github.com/moustakas/SGA/issues>.

In terms of the data reduction, the most significant known issue impacting the SGA-2020 is the pattern-noise subtraction from the Mosaic-3 imaging, which distorts the z -band surface-brightness profiles and colors of galaxies in the (northern) BASS+MzLS portion of the footprint (see § 3.2.1 for details). In addition, SGA users have reported that in some cases the WISE W1 and W2 background signal has been over-subtracted. We hypothesize that this over-subtraction arises because the unWISE background is modeled as the median flux after subtracting all the point-sources in a $1' \times 1'$ grid (Schlafly et al. 2019), which would potentially impact all galaxies in the sample larger than approximately one arcminute.

Some issues also impact the availability and accuracy of the optical photometry in the SGA-2020. The most significant problem is that the elliptical aperture photometry (and the corresponding curves of growth) reported in the individual `GROUP_NAME-largegalaxy-SGA_ID-ellipse.fits` files (see Table 4) were impacted by a catastrophic bug which rendered these measurements unusable. The data model for this file is documented in Table 5 and the impacted columns are flagged with the text “Do not use; see Appendix C.” Fortunately, however, we were able to recover the curves of growth from the surface-brightness profiles themselves, which were not affected by this bug; we record those measurements in the `ELLIPSE` HDU of the merged `SGA-2020.fits` file (as documented in Table 2).

Moreover, ellipse-fitting was skipped, failed, or rejected for a few different reasons which are encoded in the `ELLIPSEBIT` column; this column appears in Table 2 and is documented in Table 3. First, a total of 8415 galaxies were not ellipse-fit because they were deemed to be too small (`ELLIPSEBIT = 21` or `ELLIPSEBIT = 22`) via their best-fitting `Tractor` model and half-light radius (`shape_r`); specifically, objects modeled by `The Tractor` as `type=REX` with `shape_r < 2''` or `type={EXP,DEV,SER}` with `shape_r < 5''` were not ellipse-fit.³⁷ Second, ellipse-fitting did not complete (`ELLIPSEBIT = 24`) for 27 galaxies in the following seven groups: IC1613, NGC0055 Group, NGC0253 Group, NGC0300 Group, NGC0598 Group, NGC3031 Group, and NGC5457. The central galaxies in these groups rank among the largest in the sample ($18' < \text{GROUP_DIAMETER} < 62'$), so modeling these systems posed some especially acute computational challenges. Third, the ellipse-fitting results for 52 galaxies were rejected (`ELLIPSEBIT = 25`) because they were found via visual inspection to be incorrect or unreliable, usually due to incomplete or imperfect masking of nearby bright stars or other galaxies. Finally, ellipse-fitting was not carried out (or silently failed) on 6161 galaxies where the pipeline did not indicate a problem and therefore `ELLIPSEBIT = 0` for these systems even though there are no measured surface-brightness profiles.

In no particular order, some of the additional currently known issues include:

- A small number of objects without imaging in all three *grz* bandpasses (e.g., <https://sga.legacysurvey.org/group/PGC1411139>) made it into final sample, despite the requirement of three-band optical imaging discussed in §3.2;
- A small fraction of objects have compromised surface-brightness profiles due to their proximity to bright stars (e.g., <https://sga.legacysurvey.org/group/UGC09630>) or because of poor deblending of multiple sources (typically due to incompleteness in the parent HyperLeda catalog; e.g., https://sga.legacysurvey.org/group/PGC087438_GROUP).

³⁷ The `Tractor` `type` and `shape_r` measurements are fully documented at <https://www.legacysurvey.org/dr9/catalogs/#region-tractor-aaa-tractor-brick-fits>.

- The central coordinates for a small number of the largest ($> 5'$) galaxies in the SGA-2020 are incorrect by up to a few arcseconds, as discussed in §3.3;
- In a handful of spheroidal galaxies with large ellipticity ($\epsilon > 0.5$ or $b/a < 0.5$), our masking algorithm (see § 3.2.2) is too aggressive and inadvertently masks some of the outer-envelope light of the galaxy along the minor axis (e.g., <https://sga.legacysurvey.org/group/IC0941>).

Table 1. SGA-2020.fits File Contents

Extension		Data Model	
Number	Name	Documentation	Description
HDU01	ELLIPSE	Table 2	Sample metadata and ellipse-fitting results.
HDU02	TRACTOR	LS/DR9 Website ^a	The Tractor fitting results. ^b

NOTE—Catalog containing the principal measurements for all 383,620 galaxies in the SGA-2020 as a multi-extension FITS file with two row-matched Header/Data Units (HDUs).

^a<https://www.legacysurvey.org/dr9/catalogs>

^bThis table also includes SGA_ID (see Table 2) to facilitate cross-matching.

Table 2. ELLIPSE HDU Data Model

Column Name	Units	Description
SGA_ID	...	Unique integer identifier.
SGA_GALAXY	...	SGA galaxy name, constructed as “SGA-2020-SGA_ID”.
GALAXY	...	Unique galaxy name.
PGC ^a	...	Unique identifier from the <i>Principal Catalogue of Galaxies</i> .
RA_LEDA	degree	Right ascension (J2000) from the reference indicated in REF.
DEC_LEDA	degree	Declination (J2000) from the reference indicated in REF.
MORPHTYPE	...	Visual morphological type from HyperLeda (if available).
PA_LEDA	degree	Galaxy position angle (measured East of North); taken from the reference indicated in REF.
D25_LEDA	arcmin	Major-axis diameter at the 25 mag arcsec ⁻² (optical) surface brightness isophote; taken from the reference indicated in REF.
BA_LEDA	...	Ratio of the semi-minor axis to the semi-major axis; taken from the reference indicated in REF.
Z_LEDA ^a	...	Heliocentric redshift from HyperLeda.
SB_D25_LEDA	Vega mag arcsec ⁻²	Mean surface brightness based on D25_LEDA and MAG_LEDA.
MAG_LEDA ^b	Vega mag	Apparent b_t -band magnitude.
BYHAND	...	Boolean flag indicating whether one or more of RA_LEDA, DEC_LEDA, D25_LEDA, PA_LEDA, BA_LEDA, or MAG_LEDA were changed from their published values (usually via visual inspection) while building the parent sample.
REF	...	Reference indicating the origin of the object (see §2): LEDA-20181114, LGDWARFS, RC3, OpenNGC, or DR8.
GROUP_ID	...	Unique group identification number.
GROUP_NAME	...	Group name, constructed from the name of its largest member (see §2.2). For isolated galaxies, identical to GALAXY.
GROUP_MULT	...	Number of group members (i.e., group multiplicity).
GROUP_PRIMARY	...	Boolean flag indicating the primary (i.e., largest) group member.
GROUP_RA	degree	Mean right ascension of the group weighted by D25_LEDA.
GROUP_DEC	degree	Mean declination of the group weighted by D25_LEDA.

Table 2 continued on next page

Table 2 (*continued*)

Column Name	Units	Description
GROUP_DIAMETER	arcmin	Approximate group diameter (see §2.2).
BRICKNAME	...	Name of custom <code>Tractor</code> “brick”, encoding the sky position, e.g. “1126p222” is centered on RA=112.6, Dec=+22.2.
RA	degree	Right ascension (J2000) based on <code>The Tractor</code> model fit.
DEC	degree	Declination (J2000) based on <code>The Tractor</code> model fit.
D26	arcmin	Major axis diameter at the $\mu = 26$ mag arcsec ⁻² r -band isophote.
D26_REF ^c	...	Reference indicating the origin of the DIAM measurement: SB26, SB25, or LEDA.
PA	degree	Galaxy position angle (measured East of North), as measured from the <code>ellipse moments</code> (see §3.2.3) (or equivalent to PA_LEDA if the <code>ellipse moments</code> could not be measured).
BA	...	Minor-to-major axis ratio, as measured from the <code>ellipse moments</code> (or equivalent to BA_LEDA if the <code>ellipse moments</code> could not be measured).
RA_MOMENT	degree	Light-weighted right ascension (J2000), as measured from the <code>ellipse moments</code> . Equivalent to RA_X0 in Table 5 but set to RA_LEDA if ellipse-fitting failed or was not carried out.
DEC_MOMENT	degree	Like RA_MOMENT but for the declination axis.
SMA_MOMENT ^d	arcsec	Second moment of the light distribution along the major axis based on the measured <code>ellipse moments</code> . Equivalent to MAJORAXIS in Table 5 but converted to arcsec.
<grz>_SMA50 ^d	arcsec	Half-light semi-major axis length based on equation (2).
SMA_SB<sblevel> ^d	arcsec	Semi-major axis length at the r -band <sblevel> mag arcsec ⁻² isophote.
<grz>_MAG_SB<sblevel> ^d	AB mag	Cumulative brightness measured within SMA_SB<sblevel>.
<grz>_MAG_SB<sblevel>_ERR ^d	AB mag	1 σ uncertainty in <grz>_MAG_SB<sblevel>.
<grz>_COG_PARAMS_MTOT ^d	AB mag	Best-fitting curve-of-growth parameter m_1 from equation (1).
<grz>_COG_PARAMS_M0 ^d	AB mag	Best-fitting curve-of-growth parameter m_0 from equation (1).
<grz>_COG_PARAMS_ALPHA1 ^d	...	Best-fitting curve-of-growth parameter α_1 from equation (1).
<grz>_COG_PARAMS_ALPHA2 ^d	...	Best-fitting curve-of-growth parameter α_2 from equation (1).
<grz>_COG_PARAMS_CHI2 ^d	...	χ^2 of the fit to the curve-of-growth (see §3.2.3).
ELLIPSEBIT	...	See Table 3.

NOTE—ELLIPSE HDU of the SGA-2020.fits merged catalog defined in Table 1. In this table <grz> denotes the g -, r -, or z -band filter; <wise> denotes the $W1$ -, $W2$ -, $W3$ -, or $W4$ bandpass; and <sblevel> represents the 22, 22.5, 23, 23.5, 24, 24.5, 25, 25.5, and 26 mag arcsec⁻² isophote.

^aMissing values are represented with a -1 . For some quantities (e.g., PGC or Z_LEDA) a missing value does not necessarily mean that that value does not exist.

^bThis magnitude estimate is heterogeneous in both bandpass and aperture but for most galaxies it is measured in the B -band; use with care.

^cBy default, we infer D26 from SMA_SB26. However, if the r -band surface-brightness profile could not be measured at this level, we estimate D26 as $2.5 \times \text{SMA_SB25}$ or $1.5 \times \text{D25_LEDA}$, in that order of priority.

^dIf ellipse-fitting or curve-of-growth modeling failed or was not attempted then these columns’ values are -1 .

Table 3. Ellipse-Fitting Bitmasks

Bit Number	Bit Name	Definition
0	...	Not used; ignore.
1	REX_TOOSMALL	Ellipse-fit skipped; galaxy classified as too-small type REX .
2	NOTREX_TOOSMALL	Ellipse-fit skipped; galaxy classified as too-small type EXP , DEV , or SER .
3	FAILED	Ellipse-fitting was attempted but failed.
4	NOTFIT	Ellipse-fitting was not attempted.
5	REJECTED	Ellipse-fitting results were rejected based on visual inspection.

NOTE—Bitmask encoding various reasons why ellipse-fitting failed or was not attempted; see §3.2.3 for additional details.

Table 4. Images and Catalogs

Filename	Description
GROUP_NAME-ccd-⟨region⟩.fits	CCDs contributing to the optical image stacks.
GROUP_NAME-largegalaxy-blobs.fits.gz	Enumerated segmentation (“blob”) image.
GROUP_NAME-largegalaxy-tractor.fits	Tractor catalog of all detected sources in the field.
GROUP_NAME-largegalaxy-maskbits.fits.fz	Image encoding the LS/DR9 bitmasks ^a contributing to each pixel.
GROUP_NAME-largegalaxy-outlier-mask.fits.fz	Image of pixels rejected during outlier masking.
GROUP_NAME-depth-⟨grz⟩.fits.fz	Image of the 5σ point-source depth at each pixel.
GROUP_NAME-largegalaxy-psf-⟨grz⟩.fits.fz	Postage stamp of the inverse-variance weighted mean pixelized PSF at the center of the field.
GROUP_NAME-largegalaxy-image-⟨grz⟩.fits.fz	Inverse-variance weighted optical image.
GROUP_NAME-largegalaxy-invvar-⟨grz⟩.fits.fz	Optical inverse variance image stack.
GROUP_NAME-largegalaxy-model-⟨grz⟩.fits.fz	Optical Tractor model image coadd.
GROUP_NAME-largegalaxy-image-grz.jpg	Color (<i>grz</i>) JPG image of the image stack.
GROUP_NAME-largegalaxy-model-grz.jpg	Color (<i>grz</i>) JPG image of The Tractor model image.
GROUP_NAME-largegalaxy-resid-grz.jpg	Color (<i>grz</i>) JPG image of residual (data minus model) image.
GROUP_NAME-image-⟨wise⟩.fits.fz	Inverse-variance weighted infrared image stack.
GROUP_NAME-invvar-⟨wise⟩.fits.fz	Infrared inverse variance image stack.
GROUP_NAME-largegalaxy-model-⟨wise⟩.fits.fz	Infrared Tractor model image coadd.
GROUP_NAME-image-W1W2.jpg	Color (<i>W1W2</i>) JPG image of the image stack.
GROUP_NAME-model-W1W2.jpg	Color (<i>W1W2</i>) JPG image of The Tractor model image.
GROUP_NAME-largegalaxy-sample.fits	Catalog of one or more galaxies from the parent sample in this group.
GROUP_NAME-largegalaxy-SGA_ID-ellipse.fits ^b	Detailed ellipse-fitting results for each galaxy in this group; see Table 5 for the data model.
GROUP_NAME-coadds.log	Log output for the coadds stage of the SGA pipeline.
GROUP_NAME-ellipse.log	Log output for the ellipse stage of the SGA pipeline.

NOTE—Summary of files generated for each galaxy group in the SGA-2020. In this table, ⟨region⟩ denotes either **north** for BASS/MzLS or **south** for DECaLS; ⟨grz⟩ denotes the *g*-, *r*-, or *z*-band filter; and ⟨wise⟩ denotes the *W1*-, *W2*-, *W3*-, or *W4* bandpass.

^a <https://www.legacysurvey.org/dr9/bitmasks>

^b This file may be missing (for the galaxy of a given **SGA_ID**) if ellipse-fitting fails or is not carried out.

Table 5. Ellipse-Fitting Data Model

Column Name	Units	Description
SGA_ID	...	See Table 2.
GALAXY	...	See Table 2.
RA	degree	See Table 2.
DEC	degree	See Table 2.
PGC	...	See Table 2.
PA_LEDA	degree	See Table 2.
BA_LEDA	...	See Table 2.
D25_LEDA	arcmin	See Table 2.
BANDS	...	List of bandpasses fitted (here, always <i>grz</i>).
REFBAND	...	Reference band (here, always <i>r</i>).
REFPIXSCALE	arcsec pixel ⁻¹	Pixel scale in REFBAND.
SUCCESS	...	Flag indicating ellipse-fitting success or failure.
FITGEOMETRY	...	Flag indicating whether the ellipse geometry was allowed to vary with semi-major axis (here, always False).
INPUT_ELLIPSE	...	Flag indicating whether ellipse parameters were passed from an external file (here, always False).
LARGESHIFT	...	Flag indicating that the light-weighted center (from ellipse moments) is different from The Tractor position by more than 10 pixels in either dimension, in which case we adopt The Tractor model position.
RA_X0	degree	Right ascension (J2000) at pixel position X0.
DEC_Y0	degree	Declination (J2000) at pixel position Y0.
X0	pixel	Light-weighted position along the <i>x</i> -axis (from ellipse moments).
Y0	pixel	Light-weighted position along the <i>y</i> -axis (from ellipse moments).
EPS	...	Ellipticity, $\epsilon \equiv 1 - b/a$, where <i>b/a</i> is the semi-minor to semi-major axis ratio BA in Table 1.
PA	degree	Galaxy position angle (astronomical convention, measured East of North); equivalent to PA in Table 1.
THETA	degree	Galaxy position angle (physics convention, measured North of West) given by $270 - \text{PA} \bmod 180$.
MAJORAXIS	pixel	Light-weighted length of the semi-major axis (from ellipse moments).
MAXSMA	pixel	Maximum semi-major axis length used for the ellipse-fitting and curve-of-growth measurements (typically taken to be $2 \times \text{MAJORAXIS}$).
INTEGRMODE ^a	...	Integration mode (here, always <i>median</i>).
SCLIP ^a	...	Sigma-clipping threshold (here, always 3).
NCLIP ^a	...	Sigma-clipping iterations (here, always 2).
PSFSIZE_<grz>	arcsec	Mean FWHM of the point-spread function over the full mosaic (derived from the PSFSIZE_<grz> columns in The Tractor catalogs).
PSFDEPTH_<grz>	AB mag	Mean 5σ point-source depth over the full mosaic (derived from the PSFDEPTH_<grz> columns in The Tractor catalogs).
MW_TRANSMISSION_<grz>	...	Galactic transmission fraction (taken from the corresponding Tractor catalog at the central coordinates of the galaxy).
REFBAND_WIDTH	pixel	Width of the optical mosaics in REFBAND.
REFBAND_HEIGHT	pixel	Height of the optical mosaics in REFBAND.
<grz>_SMA	pixel	Ellipse semi-major axis position.
<grz>_INTENS	nanomaggies arcsec ⁻²	Linear surface brightness at <grz>_SMA.

Table 5 continued on next page

Table 5 (continued)

Column Name	Units	Description
<code><grz>_INTENS_ERR</code>	nanomaggies arcsec ⁻²	1 σ uncertainty in <code><grz>_INTENS</code> .
<code><grz>_EPS</code>	...	Ellipse ellipticity; here, fixed at EPS.
<code><grz>_EPS_ERR</code>	...	1 σ uncertainty in <code><grz>_EPS</code> .
<code><grz>_PA</code>	degree	Ellipse position angle; here, fixed at PA.
<code><grz>_PA_ERR</code>	degree	1 σ uncertainty in <code><grz>_PA</code> .
<code><grz>_X0</code>	pixel	Ellipse x -axis pixel coordinate; here, fixed at X0.
<code><grz>_X0_ERR</code>	pixel	1 σ uncertainty in <code><grz>_X0</code> .
<code><grz>_Y0</code>	pixel	Ellipse y -axis pixel coordinate; here, fixed at Y0.
<code><grz>_Y0_ERR</code>	pixel	1 σ uncertainty in <code><grz>_Y0</code> .
<code><grz>_A3^b</code>	...	Third-order harmonic coefficient; not used.
<code><grz>_A3_ERR^b</code>	...	1 σ uncertainty in <code><grz>_A3</code> .
<code><grz>_A4^b</code>	...	Fourth-order harmonic coefficient; not used.
<code><grz>_A4_ERR^b</code>	...	1 σ uncertainty in <code><grz>_A4</code> .
<code><grz>_RMS^b</code>	nanomaggies arcsec ⁻²	Root-mean-square surface brightness along the elliptical path.
<code><grz>_PIX_STDDEV^b</code>	nanomaggies	Pixel standard deviation estimate.
<code><grz>_STOP_CODE^b</code>	...	Fitting stop code.
<code><grz>_NDATA^b</code>	...	Number of data points used for the fit.
<code><grz>_NFLAG^b</code>	...	Number of points rejected during the fit.
<code><grz>_NITER^b</code>	...	Number of fitting iterations.
<code><grz>_COG_SMA</code>	pixel	Do not use; see Appendix C.
<code><grz>_COG_MAG</code>	AB mag	Do not use; see Appendix C.
<code><grz>_COG_MAGERR</code>	AB mag	Do not use; see Appendix C.
<code><grz>_COG_PARAMS_MTOT</code>	AB mag	Do not use; see Appendix C.
<code><grz>_COG_PARAMS_M0</code>	AB mag	Do not use; see Appendix C.
<code><grz>_COG_PARAMS_ALPHA1</code>	...	Do not use; see Appendix C.
<code><grz>_COG_PARAMS_ALPHA2</code>	...	Do not use; see Appendix C.
<code><grz>_COG_PARAMS_CHI2</code>	...	Do not use; see Appendix C.
<code>RADIUS_SB<sblevel></code>	arcsec	Do not use; see Appendix C.
<code>RADIUS_SB<sblevel>_ERR</code>	arcsec	Do not use; see Appendix C.
<code><grz>_MAG_SB<sblevel></code>	AB mag	Do not use; see Appendix C.
<code><grz>_MAG_SB<sblevel>_ERR</code>	AB mag	Do not use; see Appendix C.

NOTE—Ellipse-fitting results and surface-brightness profiles for a single galaxy in the SGA-2020; specifically, this table documents the data model for the `GROUP_NAME-largegalaxy-SGA_ID-ellipse.fits` file listed in Table 4. In this table `<grz>` denotes the g -, r -, or z -band filter and `<sblevel>` represents the 22, 22.5, 23, 23.5, 24, 24.5, 25, 25.5, and 26 mag arcsec⁻² isophote.

^aSee the `photutils.isophote.Ellipse.fit_image` method documentation.

^bSee the `photutils.isophote.Isophote` and `photutils.isophote.IsophoteList` method documentation.

REFERENCES

- Abareshi, B., Aguilar, J., Ahlen, S., et al. 2022, *AJ*, 164, 207. <https://arxiv.org/abs/2205.10939>
- Abbott, B. P., Abbott, R., Abbott, T. D., et al. 2020, *Living Reviews in Relativity*, 23, 3
- Abbott, T. M. C., Adamów, M., Agüena, M., et al. 2021, *ApJS*, 255, 20. <https://arxiv.org/abs/2101.05765>
- Astropy Collaboration, Robitaille, T. P., Tollerud, E. J., et al. 2013, *A&A*, 558, A33. <https://arxiv.org/abs/1307.6212>

- Astropy Collaboration, Price-Whelan, A. M., Sipőcz, B. M., et al. 2018, *AJ*, 156, 123.
<https://arxiv.org/abs/1801.02634>
- Astropy Collaboration, Price-Whelan, A. M., Lim, P. L., et al. 2022, *ApJ*, 935, 167. <https://arxiv.org/abs/2206.14220>
- Bernardi, M., Meert, A., Sheth, R. K., et al. 2013, *MNRAS*, 436, 697.
<https://arxiv.org/abs/1304.7778>
- Blanton, M. R., Kazin, E., Muna, D., Weaver, B. A., & Price-Whelan, A. 2011, *AJ*, 142, 31.
<https://arxiv.org/abs/1105.1960>
- Blanton, M. R., & Moustakas, J. 2009, *ARA&A*, 47, 159.
<https://arxiv.org/abs/0908.3017>
- Blanton, M. R., Schlegel, D. J., Strauss, M. A., et al. 2005, *AJ*, 129, 2562
- Bradley, L. 2023, *astropy/photutils: 1.8.0, 1.8.0*, Zenodo, Zenodo
- Cannon, R. D. 1979, *The U.K. 1.2m Schmidt telescope and the southern sky survey (Edinburgh : [Royal Observatory], 19)*
- Cappellari, M. 2002, *MNRAS*, 333, 400.
<https://arxiv.org/abs/astro-ph/0201430>
- Chambers, K. C., Magnier, E. A., Metcalfe, N., et al. 2016, arXiv e-prints, arXiv:1612.05560.
<https://arxiv.org/abs/1612.05560>
- Chaussidon, E., Yèche, C., Palanque-Delabrouille, N., et al. 2023, *ApJ*, 944, 107.
<https://arxiv.org/abs/2208.08511>
- Conroy, C. 2013, *ARA&A*, 51, 393.
<https://arxiv.org/abs/1301.7095>
- Corwin, Jr., H. G., Buta, R. J., & de Vaucouleurs, G. 1994, *AJ*, 108, 2128
- Dark Energy Survey Collaboration, Abbott, T., Abdalla, F. B., et al. 2016, *MNRAS*, 460, 1270.
<https://arxiv.org/abs/1601.00329>
- de Vaucouleurs, G. 1948, *Annales d'Astrophysique*, 11, 247
- de Vaucouleurs, G., de Vaucouleurs, A., Corwin, Jr., H. G., et al. 1991, *Third Reference Catalogue of Bright Galaxies. Volume I: Explanations and references. Volume II: Data for galaxies between 0^h and 12^h. Volume III: Data for galaxies between 12^h and 24^h.*
- DESI Collaboration, Aghamousa, A., Aguilar, J., et al. 2016a, ArXiv e-prints. <https://arxiv.org/abs/1611.00036>
- . 2016b, ArXiv e-prints. <https://arxiv.org/abs/1611.00037>
- DESI Collaboration, Adame, A. G., Aguilar, J., et al. 2023a, arXiv e-prints, arXiv:2306.06308.
<https://arxiv.org/abs/2306.06308>
- . 2023b, arXiv e-prints, arXiv:2306.06307.
<https://arxiv.org/abs/2306.06307>
- Dey, A., Rabinowitz, D., Karcher, A., et al. 2016, in *Society of Photo-Optical Instrumentation Engineers (SPIE) Conference Series*, Vol. 9908, Ground-based and Airborne Instrumentation for Astronomy VI, ed. C. J. Evans, L. Simard, & H. Takami, 99082C
- Dey, A., Schlegel, D. J., Lang, D., et al. 2019, *AJ*, 157, 168.
<https://arxiv.org/abs/1804.08657>
- Djorgovski, S., & Davis, M. 1987, *ApJ*, 313, 59
- Dreyer, J. L. E. 1888, *MmRAS*, 49, 1
- . 1912, *MNRAS*, 73, 37
- Ducoin, J. G., Corre, D., Leroy, N., & Le Floch, E. 2020, *MNRAS*, 492, 4768.
<https://arxiv.org/abs/1911.05432>
- Finkbeiner, D. P., Schlafly, E. F., Schlegel, D. J., et al. 2016, *ApJ*, 822, 66. <https://arxiv.org/abs/1512.01214>
- Flaugher, B., Diehl, H. T., Honscheid, K., et al. 2015, *AJ*, 150, 150.
<https://arxiv.org/abs/1504.02900>
- Foreman-Mackey, D. 2016, *The Journal of Open Source Software*, 1, 24
- Fukugita, M., Nakamura, O., Okamura, S., et al. 2007, *AJ*, 134, 579.
<https://arxiv.org/abs/0704.1743>

- Gaia Collaboration, Brown, A. G. A., Vallenari, A., et al. 2018, *A&A*, 616, A1. <https://arxiv.org/abs/1804.09365>
- Gehrels, N., Cannizzo, J. K., Kanner, J., et al. 2016, *ApJ*, 820, 136. <https://arxiv.org/abs/1508.03608>
- Gil de Paz, A., Boissier, S., Madore, B. F., et al. 2007, *ApJS*, 173, 185
- Giovanelli, R., Haynes, M. P., Salzer, J. J., et al. 1994, *AJ*, 107, 2036
- Guy, J., Bailey, S., Kremin, A., et al. 2023, *AJ*, 165, 144. <https://arxiv.org/abs/2209.14482>
- Hahn, C., Wilson, M. J., Ruiz-Macias, O., et al. 2023, *AJ*, 165, 253. <https://arxiv.org/abs/2208.08512>
- Harris, C. R., Millman, K. J., van der Walt, S. J., et al. 2020, *Nature*, 585, 357. <https://arxiv.org/abs/2006.10256>
- Helou, G., Madore, B. F., Schmitz, M., et al. 1991, in *Astrophysics and Space Science Library*, Vol. 171, Databases and On-line Data in Astronomy, ed. M. A. Albrecht & D. Egret, 89–106
- Herschel, J. F. W. 1864, *Philosophical Transactions of the Royal Society of London Series I*, 154, 1
- Herschel, W. 1786, *Philosophical Transactions of the Royal Society of London Series I*, 76, 457
- Holmberg, E. 1958, *Meddelanden fran Lunds Astronomiska Observatorium Serie II*, 136, 1
- Hunter, J. D. 2007, *Computing in Science and Engineering*, 9, 90
- Jarrett, T. H., Chester, T., Cutri, R., et al. 2000, *AJ*, 119, 2498. <https://arxiv.org/abs/astro-ph/0004318>
- Jarrett, T. H., Chester, T., Cutri, R., Schneider, S. E., & Huchra, J. P. 2003, *AJ*, 125, 525
- Jarrett, T. H., Cluver, M. E., Brown, M. J. I., et al. 2019, *ApJS*, 245, 25. <https://arxiv.org/abs/1910.11793>
- Kennicutt, Jr., R. C. 1998, *ARA&A*, 36, 189
- Kewley, L. J., Nicholls, D. C., & Sutherland, R. S. 2019, *ARA&A*, 57, 511. <https://arxiv.org/abs/1910.09730>
- Kormendy, J., & Kennicutt, Jr., R. C. 2004, *ARA&A*, 42, 603
- Kovlakas, K., Zezas, A., Andrews, J. J., et al. 2021, *MNRAS*, 506, 1896. <https://arxiv.org/abs/2106.12101>
- Lang, D. 2014, *AJ*, 147, 108. <https://arxiv.org/abs/1405.0308>
- Lang, D., Hogg, D. W., & Schlegel, D. J. 2016, *AJ*, 151, 36. <https://arxiv.org/abs/1410.7397>
- Lauberts, A. 1982, *ESO/Uppsala survey of the ESO(B) atlas (Garching: European Southern Observatory (ESO))*
- Leja, J., Johnson, B. D., Conroy, C., van Dokkum, P. G., & Byler, N. 2017, *ApJ*, 837, 170. <https://arxiv.org/abs/1609.09073>
- Leroy, A. K., Sandstrom, K. M., Lang, D., et al. 2019, *ApJS*, 244, 24. <https://arxiv.org/abs/1910.13470>
- Li, J., Huang, S., Leauthaud, A., et al. 2022, *MNRAS*, 515, 5335. <https://arxiv.org/abs/2111.03557>
- Magnier, E. A., Sweeney, W. E., Chambers, K. C., et al. 2020, *ApJS*, 251, 5. <https://arxiv.org/abs/1612.05244>
- Mainzer, A., Bauer, J., Cutri, R. M., et al. 2014, *ApJ*, 792, 30. <https://arxiv.org/abs/1406.6025>
- Makarov, D., Prugniel, P., Terekhova, N., Courtois, H., & Vauglin, I. 2014, *A&A*, 570, A13. <https://arxiv.org/abs/1408.3476>
- Makarov, D., Savchenko, S., Mosenkov, A., et al. 2022, *MNRAS*, 511, 3063. <https://arxiv.org/abs/2201.08888>
- Martin, D. C., Fanson, J., Schiminovich, D., et al. 2005, *ApJL*, 619, L1
- Mateo, M. L. 1998, *ARA&A*, 36, 435. <https://arxiv.org/abs/astro-ph/9810070>
- McConnachie, A. W. 2012, *AJ*, 144, 4. <https://arxiv.org/abs/1204.1562>
- Meert, A., Vikram, V., & Bernardi, M. 2015, *MNRAS*, 446, 3943. <https://arxiv.org/abs/1406.4179>

- Meisner, A. M., Lang, D., Schlafly, E. F., & Schlegel, D. J. 2021, *Research Notes of the American Astronomical Society*, 5, 168
- Minkowski, R. L., & Abell, G. O. 1963, in *Basic Astronomical Data: Stars and Stellar Systems*, ed. K. A. Strand (University of Chicago Press), 481
- Morrissey, P., Schiminovich, D., Barlow, T. A., et al. 2005, *ApJL*, 619, L7
- Myers, A. D., Moustakas, J., Bailey, S., et al. 2023, *AJ*, 165, 50.
<https://arxiv.org/abs/2208.08518>
- Naab, T., & Ostriker, J. P. 2017, *ARA&A*, 55, 59.
<https://arxiv.org/abs/1612.06891>
- Neronov, A. 2021, in *Journal of Physics Conference Series*, Vol. 2156, *Journal of Physics Conference Series*, 012006
- Nilson, P. 1973, *Nova Acta Regiae Soc. Sci. Upsaliensis Ser. V*
- Nilson, P. 1974, *Uppsala Astronomical Observatory Reports*, 5
- Oke, J. B., & Schild, R. E. 1970, *ApJ*, 161, 1015
- Paturel, G., Fouque, P., Bottinelli, L., & Gouguenheim, L. 1989, *A&AS*, 80, 299
- Paturel, G., Andernach, H., Bottinelli, L., et al. 1997, *A&AS*, 124, 109. <https://arxiv.org/abs/astro-ph/9806140>
- Raichoor, A., Moustakas, J., Newman, J. A., et al. 2023, *AJ*, 165, 126.
<https://arxiv.org/abs/2208.08513>
- Reid, N., & Djorgovski, S. 1993, in *Astronomical Society of the Pacific Conference Series*, Vol. 43, *Sky Surveys. Protostars to Protogalaxies*, ed. B. T. Soifer, 125
- Sánchez, S. F. 2020, *ARA&A*, 58, 99.
<https://arxiv.org/abs/1911.06925>
- Saulder, C., Howlett, C., Douglass, K. A., et al. 2023, *arXiv e-prints*, arXiv:2302.13760.
<https://arxiv.org/abs/2302.13760>
- Schlafly, E. F., Meisner, A. M., & Green, G. M. 2019, *ApJS*, 240, 30.
<https://arxiv.org/abs/1901.03337>
- Sersic, J. L. 1968, *Atlas de Galaxias Australes* (Cordoba, Argentina: Observatorio Astronomico)
- Sheth, K., Regan, M., Hinz, J. L., et al. 2010, *PASP*, 122, 1397.
<https://arxiv.org/abs/1010.1592>
- Simard, L., Mendel, J. T., Patton, D. R., Ellison, S. L., & McConnachie, A. W. 2011, *ApJS*, 196, 11.
<https://arxiv.org/abs/1107.1518>
- Skrutskie, M. F., Cutri, R. M., Stiening, R., et al. 2006, *AJ*, 131, 1163
- Somerville, R. S., & Davé, R. 2015, *ARA&A*, 53, 51.
<https://arxiv.org/abs/1412.2712>
- Stein, G., Blaum, J., Harrington, P., Medan, T., & Lukić, Z. 2022, *ApJ*, 932, 107. <https://arxiv.org/abs/2110.00023>
- Strauss, M. A., & Willick, J. A. 1995, *PhR*, 261, 271. <https://arxiv.org/abs/astro-ph/9502079>
- Strauss, M. A., Weinberg, D. H., Lupton, R. H., et al. 2002, *AJ*, 124, 1810
- Tully, R. B., & Fisher, J. R. 1977, *A&A*, 54, 661
- Valdes, F., Gruendl, R., & DES Project. 2014, in *Astronomical Society of the Pacific Conference Series*, Vol. 485, *Astronomical Data Analysis Software and Systems XXIII*, ed. N. Manset & P. Forshay, 379
- Virtanen, P., Gommers, R., Oliphant, T. E., et al. 2020, *Nature Methods*, 17, 261. <https://arxiv.org/abs/1907.10121>
- Vorontsov-Velyaminov, B., & Krasnogorskaya, A. A. 1974, *Morphological catalogue of galaxies* (Trudi Gosudarstvennovo Astronomicheskogo Instituta (Sternberg), Moscow: State University)
- Wake, D. A., Bundy, K., Diamond-Stanic, A. M., et al. 2017, *AJ*, 154, 86.
<https://arxiv.org/abs/1707.02989>
- Walmsley, M., Lintott, C., Géron, T., et al. 2022, *MNRAS*, 509, 3966.
<https://arxiv.org/abs/2102.08414>
- Waskom, M. 2021, *The Journal of Open Source Software*, 6, 3021
- Weaver, B. A., Robitaille, T., Tollerud, E., et al. 2019, *weaverba137/pydl: Last Python 2 Release, 0.7.0*, Zenodo, Zenodo

- Wechsler, R. H., & Tinker, J. L. 2018, *ARA&A*, 56, 435. <https://arxiv.org/abs/1804.03097>
- Wenger, M., Ochsenbein, F., Egret, D., et al. 2000, *A&AS*, 143, 9. <https://arxiv.org/abs/astro-ph/0002110>
- Williams, G. G., Olszewski, E., Lesser, M. P., & Burge, J. H. 2004, in *Society of Photo-Optical Instrumentation Engineers (SPIE) Conference Series*, Vol. 5492, Ground-based Instrumentation for Astronomy, ed. A. F. M. Moorwood & M. Iye, 787–798
- Wright, E. L., Eisenhardt, P. R. M., Mainzer, A. K., et al. 2010, *AJ*, 140, 1868. <https://arxiv.org/abs/1008.0031>
- York, D. G., Adelman, J., Anderson, Jr., J. E., et al. 2000, *AJ*, 120, 1579
- Zaritsky, D., Donnerstein, R., Dey, A., et al. 2023, arXiv e-prints, arXiv:2306.01524. <https://arxiv.org/abs/2306.01524>
- Zhou, R., Dey, B., Newman, J. A., et al. 2023, *AJ*, 165, 58. <https://arxiv.org/abs/2208.08515>
- Zonca, A., Singer, L., Lenz, D., et al. 2019, *Journal of Open Source Software*, 4, 1298
- Zou, H., Zhou, X., Fan, X., et al. 2017, *PASP*, 129, 064101. <https://arxiv.org/abs/1702.03653>
- Zwicky, F., Herzog, E., & Wild, P. 1968, *Catalogue of galaxies and of clusters of galaxies* (Pasadena: California Institute of Technology (CIT))